Journal of Spacecraft and Rockets, Available online 18 August 2021
DOI: 10.2514/1.A34986

CubeSat Autonomous Navigation and Guidance for Low-cost Asteroid Flyby Missions

Pablo Machuca* and Joan-Pau Sánchez†

Cranfield University, Bedfordshire MK43 0AL, United Kingdom

ABSTRACT

Recent advancements in CubeSat technology unfold new mission ideas and the opportunity to lower the cost of space exploration. Ground operations costs for interplanetary CubeSats, however, still represent a challenge towards low-cost CubeSat missions: hence, certain levels of autonomy are desirable. The feasibility of autonomous asteroid flyby missions using CubeSats is assessed here, and an effective strategy for autonomous operations is proposed. The navigation strategy is composed of observations of the Sun, visible planets, and the target asteroid, whereas the guidance strategy is composed of two optimally-timed trajectory correction maneuvers. A Monte Carlo analysis is performed to understand the flyby accuracies that can be achieved by autonomous CubeSats, in consideration of errors and uncertainties in: (a) departure conditions, (b) propulsive maneuvers, (c) observations, and (d) asteroid ephemerides. Flyby accuracies better than ±100 km (3σ) are found possible, and main limiting factors to autonomous missions are identified, namely: (a) on-board asteroid visibility time ($V_{lim} \geq 11$), (b) ΔV for correction maneuvers (>15 m/s), (c) asteroid ephemeris uncertainty (<1000 km), and (d) short duration of transfer to asteroid. Ultimately, this study assesses the readiness level of current CubeSat technology to autonomously flyby near-Earth asteroids, in consideration of realistic system specifications, errors and uncertainties.

Keywords:

Autonomous navigation and guidance; Interplanetary CubeSats; Near-Earth asteroids; Sun-Earth Lagrange points

*Ph.D. Candidate, School of Aerospace, Transport and Manufacturing, Building 83
†Lecturer, School of Aerospace, Transport and Manufacturing, Building 83

Nomenclature

Symbols

$\underline{\boldsymbol{A}}$	Jacobian matrix of equations of motion
ε, θ	Elevation and azimuth representing direction vectors
G	Universal gravitational constant
γ_1, γ_2	Cumulative angular errors
H	Absolute magnitude
$\underline{\boldsymbol{I}}_{ixi}$	Identity matrix of size i
m	Mass variable
$\underline{\boldsymbol{P}}$	Navigation covariance matrix
$\underline{\boldsymbol{\phi}}$	State-transition matrix
$\underline{\boldsymbol{Q}}_a$	Covariance matrix associated to event a
σ_a	Standard deviation of variable a
$\underline{\boldsymbol{T}}$	Least-squares estimator observation matrix
t	Time variable
r_s	Sum of distances from observer to pair of planets
θ_s	Angle between lines of sight from observer to pair of planets
$\boldsymbol{U}_n$	n-dimensional spherically-distributed random unit vector
V	Visual magnitude
V_{lim}	Limiting visual magnitude of navigation camera
$\boldsymbol{x} = [\boldsymbol{r}^T, \boldsymbol{v}^T]^T$	State vector (position and velocity)
$\underline{\mathbf{0}}_{ixi}$	Zero matrix of size i
bold	Represents vectors
$\underline{\boldsymbol{bold}}$	Represents matrices

Subscripts and superscripts

$(.)_i$	Variable corresponding to planetary body i

1. Introduction

Spacecraft navigational autonomy was identified as a crucial enabling technology for space exploration back in the 1990–1999 decade [1–3]. Since then, several deep-space missions have featured various levels of autonomy, including the noteworthy integration of NASA's Autonomous Optical Navigation (AutoNav) system [4] in missions such as Deep Space 1 [5], Stardust [6] and Deep Impact [7], and the successful JAXA missions Hayabusa [8] and Hayabusa2 [9].

In the past decade, efforts for the improvement of autonomous navigation capabilities have continued, employing observations of visible celestial bodies [10–13], observations of the Sun [14,15], distant stars [16,17], X-ray pulsar-based observations [18–20], and close-proximity observations of small bodies [21–25]. With the recent emergence of low-cost small-spacecraft technology, autonomous deep-space navigation is once again essential to reduce ground operations and overall mission costs.

However, only a few small-spacecraft mission concepts can be found in literature leveraging autonomous deep-space navigation—although none of which has yet been funded for implementation—namely: the SRMSAT-2 86-kg small-spacecraft study to orbit the Moon [26,27], the BIRDY 3U CubeSat study on a transfer trajectory to Mars [28], the DustCube 3U CubeSat mission proposal to the Didymos binary asteroid system [29], the LOGIC-X 12U CubeSat mission proposal in close proximity to an asteroid [30], and the LUMIO 12U CubeSat study around the Earth-Moon second Lagrange point [31].

In the context of a growing need for autonomy in deep-space small-spacecraft missions, this paper contributes with the feasibility analysis of an autonomous asteroid flyby mission using CubeSats. A strategy for autonomous navigation and guidance is proposed, main system implications for autonomous flyby missions are discussed, and the effect of system specifications on the feasibility of the mission is evaluated. The proposed navigation strategy is composed of observations of the Sun, visible planets, and of the target asteroid, and the guidance strategy consists of two optimally-timed trajectory correction maneuvers. A flexible, real-time heuristic approach to autonomously determine the most suitable time of execution of correction maneuvers is also proposed (instead of implementing pre-scheduled or fixed-navigation-accuracy maneuvers).

The baseline mission scenario leverages asteroid flyby trajectories previously computed in [32], which are compatible with current CubeSat propulsive capabilities. These flyby trajectories were designed from halo orbits around the first and second Sun-Earth Lagrange points, and a total of 36 asteroids can be reached with 80 m/s of ΔV between years 2019 and 2030 (suitable even for 3U CubeSats). The present work further explores the feasibility of performing autonomous navigation and guidance along these trajectories in the interest of an overall low-cost asteroid flyby mission. The methodology, nonetheless, is applicable to any kind of high-energy deployment opportunity as long as the mission is composed of (1) a deep-space navigation phase,

and (2) a relative navigation phase: e.g., piggyback opportunity into cislunar space or a dedicated launch into an Earth-escape trajectory.

A preliminary analysis on autonomous operations along some of these flyby trajectories was already performed in [33], and showed flyby accuracies better than 1000 km (3σ) were possible for 6 out of 24 analyzed asteroids. Analysis identified main challenges to the mission concept (e.g., limiting magnitude of the navigation camera), but a simple strategy for autonomy was employed (e.g., only one trajectory correction maneuver) and asteroid ephemeris uncertainties were not considered. A requirement of 15 was also imposed on the limiting magnitude of the navigation camera for earlier detection of target asteroids, which represents a demand far beyond the capabilities of state-of-the-art off-the-shelf attitude determination and control system (ADCS) units (limiting magnitudes of 7 in nominal operation mode [34]), and more capable CubeSat-compatible star trackers would also require exposure times in the order of 20 seconds to achieve such a limiting magnitude [35].

In an effort to relax system requirements and improve the viability of the mission, the present work takes a closer look into autonomous CubeSat operations along asteroid flyby trajectories, and a broader analysis on how system specifications affect accuracies in autonomous flyby missions is also performed. Thus, a more effective guidance strategy composed of two trajectory correction maneuvers (TCMs) is proposed, which can achieve flyby accuracies better than 100 km (3σ) for a larger number of asteroids while considering uncertainties in asteroid ephemerides and more realistic system requirements. Also, the effect of total ΔV budget and navigation camera capabilities on the resulting flyby accuracies is explored. And the scenario of a semi-autonomous mission with minimal ground support is as well investigated.

The baseline mission scenario is introduced in Section 2, modeling of errors and uncertainties is described in Section 3, the strategy for autonomous navigation and guidance is presented in Section 4, and analysis and discussion are found in Section 5.

2. Mission Scenario

The baseline mission scenario assumes a CubeSat is initially parked in a halo orbit around the first or the second Sun-Earth Lagrange points. Short transfer trajectories to near-Earth asteroids (<150 days) at ΔV costs that are compatible even with 3U platforms (<80 m/s) appear from the Sun-Earth L1/L2 points [32,33]. As such, future piggyback opportunities to L1/L2 present an interesting opportunity for the design of low-cost asteroid exploration missions. Other high-energy piggyback opportunities, or even a dedicated launch, could also enable asteroid flyby missions using small spacecraft: for instance, a deployment into cislunar space [36], or insertion into an Earth-escape trajectory [37,38]. Such deployments, however, may require longer mission durations [37], more complex trajectory designs, such as Moon flybys [36], or a larger ΔV capability [38,39]. Although this study specifically considers a deployment around L1/L2, the methodology presented here is applicable to asteroid flyby

trajectories in general, regardless of the deployment opportunity, as long as the mission is composed of a deep-space navigation phase and a relative navigation phase.

Periodic orbits around the Sun-Earth L1/L2 points, such as halo and Lissajous orbits, are commonly used by large scientific missions to study the Sun and outer space [40–44]. In fact, several missions to L1/L2 will be launched in the upcoming years and could provide a piggyback opportunity for an asteroid-flyby CubeSat mission: e.g., ESA's ARIEL [45] and PLATO [46], or NASA's WFIRST [47] and James Webb Space Telescope [48]. As a representative example of potential high-energy CubeSat deployments in the near future, analysis in the present work focuses on the feasibility of autonomous operations along asteroid flyby trajectories from L1/L2 (Fig. 1): from halo orbits ~500,000 km x 1,500,000 km x 800,000 km in size, equivalent to those of James Webb Space Telescope, ARIEL, PLATO, etc.

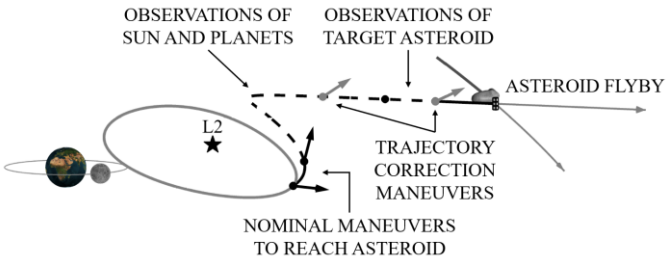

Fig. 1. Mission concept for asteroid flyby from halo orbit around second Sun-Earth Lagrange point.

The proposed strategy for autonomous navigation consists in collecting observations of: (a) the Sun, (b) visible planets, and (c) the target asteroid (Section 4.1). These observations are assumed to be collected through a coarse sun sensor (observations of the Sun), and through a star tracker (working as navigation camera for observations of visible planets and target asteroid). Both sensors could seamlessly be implemented on a 3U or larger CubeSat as part of a fully-integrated ADCS unit or as part of the science payload [33]. It may also be noted that a coarse sun sensor (e.g., 1-deg 3σ accuracy) may only support the on-board navigation process when no planets are visible by the CubeSat, since it can only provide estimation accuracies in the order of 10^6 km at a distance of ~1 au from the Sun, which is one or two orders of magnitude worse than the accuracy that can be obtained through observations of visible planets.

The proposed guidance strategy is composed of two trajectory correction maneuvers, whose time of execution, magnitude and direction are autonomously decided on board (Section 4.2). The first correction maneuver is executed prior to on-board asteroid detection, and the second correction maneuver is executed during the relative optical navigation phase. Both maneuvers have the goal of minimizing B-plane deviations from the nominal flyby [49]. In order to limit the on-board computational demand, guidance and navigation algorithms are also based only on: (a) navigation covariance matrices, and (b) state transition matrices along the reference trajectories of the CubeSat and the asteroid (which could be pre-stored in the on-board computer). This avoids numerical integration of equations of motion and complex optimization routines to time and compute TCMs.

The high-impulse asteroid flyby trajectories designed in [32] are used here as reference, nominal trajectories (Fig. 1). Flyby trajectories to 36 different asteroids from halo orbits around L1/L2 are presented in [32] (listed in Table 1); such asteroids are reached through up to two propulsive maneuvers and with less than 80 m/s in total (note that the same ΔV capability is considered here for the baseline scenario—Table 2). Targeted asteroids are all larger than ~100 meters in diameter (i.e., absolute magnitude $H \leq 22.5$), and their flyby trajectories are designed from 9 different departure points along the halo orbit: equispaced along one orbital period (e.g., Fig. 1 illustrates one of these departure points).

Out of those 36 asteroids, this present study only analyzes asteroids that are reachable with less than 75 m/s of ΔV, so that at least 5 m/s are available for TCMs, and only asteroids that can be detected more than 6 hours before the flyby are considered (important for relative navigation). The time of asteroid detection is dependent on the capabilities of the navigation camera (i.e., limiting visual magnitude V_{lim}), and so the number of analyzed asteroids is also dependent on the assumed V_{lim}. Various capabilities are employed throughout this study, from $V_{lim}=7$ to $V_{lim}=15$ (Section 5.3), with a baseline limiting magnitude $V_{lim}=11$ (Table 2 and Section 5.2). Listed in Table 1 are all of the asteroids analyzed through this study.

Table 1
List of reachable asteroids from L1/L2 [32].

	Asteroid name					
Considered in this study ($\Delta V \leq 75$ m/s, $V_{lim}=15$)	1989 JA	1997 NC1	1998 ST27	1999 AN10	2001 FO32	2001 SQ3
	2001 WN5	2004 MN4	2004 OB	2004 UE	2005 WD	2006 YT13
	2007 ML24	2008 AG33	2008 DG5	2008 GO20	2008 TZ3	2009 BL71
	2010 JG	2010 PK9	2010 XC15	2011 LJ19	2012 EY11	2014 HK129
	2015 BK509	2015 JD1	2016 AJ193	2017 XC62	2018 CC14	
Not analyzed	1997 XF11	1998 HH49	2001 XP31	2009 XO	2011 GA	2012 KY3
	2015 DG200					

Because all of the targeted near-Earth asteroids have close encounters with Earth (<0.1 au), ground-based observations of these asteroids are likely to be available prior to the CubeSat's mission. As such, it is also assumed that new ground-based astrometric observations are collected to improve the accuracy of asteroid ephemerides if the target asteroid is observable from Earth prior to L1/L2 departure (Section 3.4). As shown in Section 5.1, a ground-based observation campaign prior to the mission is particularly relevant for asteroids that have not been observed from Earth for long periods of time, and whose *a priori* ephemeris uncertainties are large (>1000 km).

Subsystem and component specifications relevant to the analysis include those of: (1) attitude determination and control system, (2) star tracker, (3) coarse sun sensor, and (4) propulsion system. The performance assumed for the baseline mission scenario is summarized in Table 2, along with a sample selection of readily-available components (applicable to 3U/6U CubeSats [33]). Please refer to Sections 5.3 and 5.4 for an extended analysis on how different scenarios and system specifications affect the feasibility of the mission. Also, note the selection of mN-level high-impulse thrusters rather than μN-

level low-thrust propulsion systems, which proves essential to autonomous missions: a low-thrust propulsion system may not be able to fully correct the trajectory given the short-duration relative navigation phases (in the order of a few days—Section 3.2.1).

Table 2
Component selection and assumed performance for baseline 3U/6U CubeSat mission.

Component	Assumed performance		Comments
	Characteristic	**Value**	
BCT's 0.5U XACT unit	Pointing knowledge	±0.01 deg (3σ)	Reported cross-axis knowledge of star tracker integrated in BCT's XACT is ±0.006 deg (3σ) [34].
	Pointing accuracy	±0.1 deg (3σ)	Reported cross-axis accuracy in low-Earth orbit (LEO) is ±0.006 deg (3σ) [50]. Conservative value of ±0.1 deg (3σ) is employed here, which could account for the unavailability of magnetometers and magnetorquers in deep space.
Micro Advanced Stellar Compass	Limiting magnitude	11	Reported limiting magnitude of star tracker integrated in BCT's XACT is 7.0 in standard operating mode (sub-second exposure times [34]). A value of 11 is derived here as a systems requirement, which could be achieved by Micro Advanced Stellar Compass (and a dedicated data processing unit) in one-second exposure times [35]. Such a star tracker (5 cm x 5 cm x 5 cm) could either substitute the one in BCT's XACT unit (5 cm x 5 cm x 10 cm [34]), or be implemented as part of the science payload. Also, jitter of BCT's XACT unit: <0.02-deg (10 s^{-1}) 3σ [50], is contained at sub-pixel level of the star tracker's CCD [51].
	Centroiding accuracy	±0.01 deg (3σ)	Pointing accuracy of non-stellar objects (e.g., asteroids, planets or satellites) is reported to be better than ±0.001 deg (3σ) [35,52]. Conservative value of ±0.01 deg (3σ) is assumed for observations of planets and of the target asteroid.
Hyperion Technologies' sun sensor	Accuracy	±1 deg (3σ)	Reported accuracy is <1 deg (3σ) [53].
For 3U design: VACCO's 5-mN 0.5U Propulsion Unit for CubeSats (80 m/s) For 6U design: VACCO's 400-mN 3U Green Propulsion System (275 m/s)	ΔV magnitude accuracy	±1% (3σ)	Note that no accuracy specification is reported for VACCO's Green Propulsion system, and VACCO's PUC reported uncertainty is <5% (3σ), but it includes experimental measurement errors (D. Carroll at CU Aerospace, personal communication, April 23, 2018). An accuracy of 1% (3σ) is derived here as a systems requirement, which can be achieved by similar mN thrusters (E. Zorzolli at ThrustMe, personal communication, July 3, 2020). If this requirement cannot be attained, a larger ΔV should be allocated for TCMs (e.g., on a 6U CubeSat—Section 5.3).
	ΔV directional accuracy	±0.1 deg (3σ)	No flutter (directional) noise is reported for VACCO's propulsion systems, but a ±0.1 deg (3σ) accuracy is derived here as a systems requirement. Such an accuracy was reported for LISA Pathfinder's μN cold gas thrusters [54] and can be achieved by similar mN thrusters (E. Zorzolli at ThrustMe, personal communication, July 3, 2020).

3. Modeling of Errors and Uncertainties

Monte Carlo simulations are performed to understand the flyby accuracies that can be achieved by an autonomous CubeSat (analysis in Section 5). The strategy for autonomy employed by the CubeSat is that described in Section 4, with the purpose of

mitigating the errors and uncertainties involved in the problem (i.e., to maximize resulting flyby accuracies). Errors and uncertainties introduced in the analysis include: (1) uncertainties in the CubeSat's initial position and velocity, (2) errors in the propulsive maneuvers, (3) errors in the observations of the Sun, planets and target asteroid, and (4) uncertainties in the trajectory of the asteroid. Analysis in Section 5.3 also discusses the impact of radiometric observations for a semi-autonomous mission, whose error modeling is also described here.

The coordinate system employed throughout the analysis is the Sun-centered J2000 Cartesian reference frame, although auxiliary reference frames are employed when convenient, to express, for instance, uncertainties in the initial state or errors in propulsive maneuvers. Also, trajectories are propagated in an ephemeris dynamical model (JPL DE403—Eq. (1)), in consideration of the gravitational influences of the Sun, Earth, Moon, and all other planets in the Solar System. Consideration of the Earth and Moon as two independent bodies (and not as a barycenter) is seen particularly relevant to accurately propagate the trajectories of the target near-Earth asteroids (i.e., since they have close encounters with Earth).

$$\frac{d\boldsymbol{v}}{dt} = \frac{d^2\boldsymbol{r}}{dt^2} = -G\sum_{i=1}^{n} m_i \cdot (\boldsymbol{r} - \boldsymbol{r}_i)/|\boldsymbol{r} - \boldsymbol{r}_i|^3 \tag{1}$$

It is further highlighted that solar radiation pressure is not included in the dynamical system, but it is argued that this does not compromise the validity of the analysis and results in the following sections. Notice that, over the course of ~100 days, the acceleration due to solar radiation pressure (in the order of 10^{-7} m/s^2) will result in perturbations in flyby position of a few thousand kilometers. These perturbations, however, are one order of magnitude smaller than the errors introduced by propulsive maneuvers and initial state uncertainties (see Section 5.2), and so they will have a minor effect on TCM requirements and estimations. Furthermore, the deterministic component of solar radiation pressure could be modeled in the computation of reference trajectories, and also included in the dynamics employed by the on-board navigation algorithms: thus refining the computation of TCMs. As for the non-deterministic components of solar radiation pressure, these are expected to be several orders of magnitude smaller than errors introduced by propulsive maneuvers and initial state uncertainties, they would be partially estimated by the on-board navigation, and they could be further included in the estimation process as additional state variables to be estimated [55].

3.1. Uncertainty in Initial State

The uncertainty in the initial state is assumed to be 30 km (3σ) in position, and 30 cm/s (3σ) in velocity. These values are drawn from the autonomous navigation study for the 12U mission LUMIO around the second Earth-Moon Lagrange point [56]. However, these accuracies may or may not be attainable by an autonomous 3U/6U CubeSat around the Sun-Earth Lagrange points (left for future work). The initial state uncertainty is derived here as a requirement for the mission, regardless of whether

it can be achieved fully autonomously or through ground support. Notice also that accuracies more than three orders of magnitude better could be achieved through ground support (Section 3.5).

The uncertainties in the initial position and velocity are described by means of an auxiliary spherical coordinate system (centered at the nominal initial state of the CubeSat), in which the initial uncertainty can be conveniently expressed by one radial and two angular uncertainties. The radial uncertainty is characterized by the corresponding normally-distributed uncertainty in position or velocity, and the two angular uncertainties are defined as uniform random errors spanning over a whole sphere. As a result, the (uncorrelated) initial covariance matrices in position and velocity are described as $\underline{\boldsymbol{P}}_{\boldsymbol{rr}}(t_0) = \left(\frac{10\ km}{\sqrt{3}}\right)^2 \cdot \underline{\boldsymbol{I}}_{3x3}$ and $\underline{\boldsymbol{P}}_{\boldsymbol{vv}}(t_0) = \left(\frac{10\ cm/s}{\sqrt{3}}\right)^2 \cdot \underline{\boldsymbol{I}}_{3x3}$ in inertial Cartesian coordinates. Note that the denominator $\sqrt{3}$ appears from projecting the radial uncertainty onto three independent axes: the covariance of an n-dimensional spherically-distributed unit random vector $\boldsymbol{U}_n$ is $Cov(\boldsymbol{U}_n) = \frac{1}{n}\underline{\boldsymbol{I}}_{nxn}$ [57].

3.2. Error in Propulsive Maneuvers

Errors in the propulsive maneuvers are modeled based on the component performance specified in Table 2. Propulsive maneuvers are modeled as impulsive and have errors both in magnitude and in direction. The magnitude error is driven by the normally-distributed magnitude accuracy of the thruster, and the direction error is cumulative and due to (1) pointing accuracy of the attitude determination and control system, and (2) directional accuracy of the thruster (Fig. 2). Both angular errors, γ_1 and γ_2, are normally distributed.

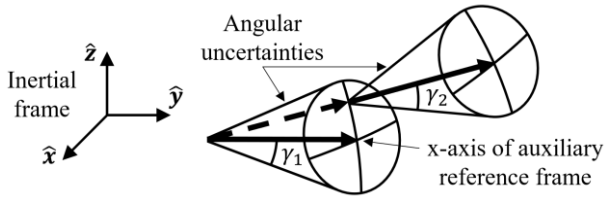

Fig. 2. Illustration of directional error due to two cumulative angular errors.

Uncertainties in the propulsive maneuvers also introduce uncertainties in the estimation of the CubeSat's trajectory. These uncertainties are accounted for as process noise by the on-board navigation algorithm (Section 4.1), according to Gates model [58], and only considering proportional errors to the magnitude of the maneuver: i.e., no bias. This process noise, $\underline{\boldsymbol{Q}}_{man}$, is assumed to influence only the velocity components of the CubeSat's covariance matrix (Eq. (2)).

$$\underline{\boldsymbol{Q}}_{man} = \begin{bmatrix} \underline{\boldsymbol{Q}}_{man,\boldsymbol{rr}} & \underline{\boldsymbol{Q}}_{man,\boldsymbol{rv}} \\ \underline{\boldsymbol{Q}}_{man,\boldsymbol{vr}} & \underline{\boldsymbol{Q}}_{man,\boldsymbol{vv}} \end{bmatrix} = \begin{bmatrix} \underline{\boldsymbol{0}}_{3x3} & \underline{\boldsymbol{0}}_{3x3} \\ \underline{\boldsymbol{0}}_{3x3} & \underline{\boldsymbol{Q}}_{man,\boldsymbol{vv}} \end{bmatrix} \tag{2}$$

Computation of matrix $\underline{\boldsymbol{Q}}_{man,vv}$ involves representing the matrix in some auxiliary reference frame and then rotating that matrix into the inertial reference frame. The auxiliary Cartesian reference frame employed here has its x-axis aligned with the direction vector of the nominal maneuver (Fig. 2), and the y- and z-axes are normal to the maneuver.

In this auxiliary reference frame, matrix $\underline{\boldsymbol{Q}}_{man,vv}$ can be expressed as in Eq. (3) (including only first-order terms, and assuming uncorrelated angular errors) [58,59].

$$\underline{\boldsymbol{Q}}_{man,vv} = |\Delta \boldsymbol{v}_{man}|^2 \cdot \begin{bmatrix} \sigma_{mag}^2 & 0 & 0 \\ 0 & \sigma_\gamma^2 & 0 \\ 0 & 0 & \sigma_\gamma^2 \end{bmatrix} \tag{3}$$

where $|\Delta \boldsymbol{v}_{man}|$ is the magnitude of the nominal propulsive maneuver, σ_{mag} is the per-one standard deviation in the magnitude of the maneuver, and $\sigma_\gamma^2 = \left(\sigma_{\gamma_1}/\sqrt{2}\right)^2 + \left(\sigma_{\gamma_2}/\sqrt{2}\right)^2$ is the cumulative angular variance due to ADCS pointing error and directional error of the thruster. Note that the denominator $\sqrt{2}$ appears from projecting the angular errors onto two independent axes (auxiliary axes y and z) [57].

3.2.1. Note on Validity of Impulsive Maneuver Model

Validity of an impulsive maneuver model for the design of high-impulse asteroid flyby trajectories using CubeSats was already verified in [32]. It was shown that the two nominal maneuvers to reach asteroids from L1/L2 can be modeled as impulsive despite long execution times and duty-cycling requirements of CubeSat thrusters: e.g., VACCO's 5-mN PUC may require up to 35 hours (~1.5 days) to generate its 80 m/s of ΔV on a 3U platform (4 kg), and VACCO's 400-mN Green Propulsion System would require up to 6 hours on a 6U CubeSat (12 kg). Analysis also showed that errors induced by an impulsive model in the calculation of VACCO's PUC ΔV requirements are generally below 1.5 m/s, compared to high-fidelity thrusting models. It is thus argued that an impulsive maneuver model holds as a valid approximation for the nominal maneuvers and for the TCM during the deep-space navigation phase (see Fig. 1), both for 3U and, especially, for 6U high-impulse missions, which require fewer hours to generate a total of 80 m/s.

It should be noted, however, that the non-instantaneity of propulsive maneuvers becomes more relevant to the TCM during the relative navigation phase. Considering an extreme case in which the full 80 m/s of ΔV are required to correct the trajectory, VACCO's PUC on a 3U CubeSat would need 1.5 days to execute such a maneuver, which is already commensurate to the duration of the relative navigation phase. For such a case, it is likely that a 3U CubeSat would need to begin correcting its trajectory shortly, and continuously, after asteroid detection. Worse yet, a low-thrust propulsion system (e.g., 100 μN) would be able to generate less than 10 m/s of ΔV during a few-day relative navigation phase.

An impulsive maneuver model is therefore a poor representation for the relative navigation phase of high-impulse and low-thrust 3U missions, whereas it may be a better approximation for a high-impulse 6U mission (i.e., 6 hours to generate a worst-case 80 m/s of ΔV). Note that in-depth evaluation of the validity of this approximation is left for future work, as well as the development of a feasible guidance strategy for low-thrust propulsion systems. Nevertheless, it is argued that an impulsive model can still serve as a useful preliminary tool to identify high-impulse mission requirements, to discuss main challenges for autonomy, and to assess the impact of different system specifications on the feasibility of autonomous flyby missions. Furthermore, as concluded in Section 5, a 3U mission shows severe limitations that encourage the use of a 6U platform (or larger), for which an impulsive model provides better approximations.

3.3. Error in On-board Observations

On-board observations are assumed to be collected by two different instruments: sun sensor and navigation camera (i.e., in this study, the star tracker). Both instruments provide directional information (i.e., two angles) of the observed bodies from the CubeSat. On the one hand, errors in the direction of the Sun are cumulative and due to (1) pointing knowledge of the ADCS, and (2) accuracy of the sun sensor. On the other hand, errors in the direction of the planets and of the target asteroid are also cumulative and due to (1) pointing knowledge of the ADCS, and (2) centroiding accuracy of the navigation camera. All directional errors are normally distributed and accumulated as represented in Fig. 2.

Uncertainties in the observations directly impact the quality of on-board navigation, which is accounted for by the observation-error covariance matrix $\underline{\boldsymbol{Q}}_{obs}$. In order to calculate this matrix, first, it is necessary to specify how direction vectors from the CubeSat to the observed bodies are represented. Direction vectors are here described by two angles: azimuth and elevation. The azimuth angle, θ, is contained in the inertial x-y plane and defined with respect to the inertial x-axis, and the elevation angle, ε, is defined with respect to the inertial x-y plane.

This selection of angles results in an observation-error covariance matrix such as that described in Eq. (4) [58,59] in inertial Cartesian coordinates.

$$\underline{\boldsymbol{Q}}_{obs} = \begin{bmatrix} \sigma_\theta^2 & \sigma_{\theta\varepsilon} \\ \sigma_{\varepsilon\theta} & \sigma_\varepsilon^2 \end{bmatrix} = \begin{bmatrix} \left(\sigma_\gamma / \cos(\varepsilon)\right)^2 & 0 \\ 0 & \sigma_\gamma^2 \end{bmatrix} \tag{4}$$

where σ_γ is defined as in Section 3.2 but substituting the observations' cumulative angular errors instead: for instance, for sun sensor observations, σ_{γ_1} and σ_{γ_2} should take the values of ADCS pointing knowledge and sun sensor accuracy. Note that the denominator $\cos(\varepsilon)$ in the azimuthal component appears from projecting the cumulative angular error onto a circle of constant elevation ε. Such a denominator also represents that only poor azimuth information can be retrieved at large elevation angles

due to the singularity in the selected Euler angle representation. However, given that the trajectories of the CubeSat, planets and asteroids are all close to the ecliptic plane, ε-values shall remain small.

3.4. Uncertainty in Asteroid Ephemeris

Asteroid ephemerides are retrieved through JPL's Horizons telnet interface [60] and propagated in time in an ephemeris dynamical model (Eq. (1)). Uncertainties in these trajectories are obtained through ESA's NEODyS-2 website [61] in the form of covariance matrices, $\underline{\boldsymbol{P}}$. These covariance matrices are provided at predetermined dates, and, in this study, they are linearly propagated in time (for instance, from time t_1 to t_2) through the state-transition matrix associated to the asteroids' nominal, reference trajectories (Eq. (5)).

$$\underline{\boldsymbol{P}}(t_2) = \underline{\boldsymbol{\phi}}(t_2, t_1) \cdot \underline{\boldsymbol{P}}(t_1) \cdot \underline{\boldsymbol{\phi}}(t_2, t_1)^T \tag{5}$$

As a note, linear propagation of covariance matrices was validated by comparing the covariance matrices provided by NEODyS at two different dates to those obtained through Eq. (5). It is observed that differences of at most 5% are obtained in the elements of the covariance matrices, even when t_1 and t_2 are several years apart.

The state-transition matrix $\underline{\boldsymbol{\phi}}$ is numerically integrated along time according to the differential equation in Eq. (6), with the identity matrix as initial condition, and with the Jacobian matrix $\underline{\boldsymbol{A}}$ defined as the partial derivatives of the equations of motion in Eq. (1) with respect to state vector $\boldsymbol{x}$.

$$\frac{d\underline{\boldsymbol{\phi}}(t, t_1)}{dt} = \underline{\boldsymbol{A}}(t) \cdot \underline{\boldsymbol{\phi}}(t, t_1) \tag{6}$$

As mentioned in Section 2, if the target asteroid can be observed from Earth prior to departure from L1/L2, then new ground-based astrometric observations are assumed to be collected to reduce uncertainties in asteroid ephemeris. Observability from Earth is determined if the visual magnitude of the asteroid is below or equals 22: V≤22 (visual magnitudes are computed based on standard photometric models [62,63]). For reference, follow-up observations of near-Earth asteroids at visual magnitudes above 22 are within the capabilities of observatory networks such as the European Southern Observatory [64], and a ground-based observation campaign could be allocated at virtually no cost [65]. A solar exclusion angle of 50 degrees is also imposed on these observations, based on the solar angle of previously-reported observations of asteroids larger than 100 m passing within 0.1 au from Earth [61]: i.e., similar characteristics to those of the targeted near-Earth asteroids.

Based on the statistical analysis of ground-based asteroid observations in [66], an accuracy of 0.388 arcsec (3σ) is assumed here for new CCD observations of asteroids, with an observation-error covariance matrix such as that in Eq. (4). For this ground-based observation campaign, one observation per day over up to ten days is assumed to be collected over the last ground-based observation window prior to L1/L2 departure. These new observations provide angular information of the target

asteroid as observed from Earth and are processed by a standard least-squares estimator [67], using as *a priori* estimation the state vector and the covariance matrix provided by NEODyS (propagated in time until the corresponding observation window—Eq. (5)).

These updated asteroid ephemerides are then employed by the CubeSat's on-board computer as *a priori* estimation during the relative navigation phase. On-board observations of the asteroid are collected by the navigation camera every 30 minutes, starting 30 minutes after the asteroid becomes visible by the CubeSat: i.e., when its visual magnitude becomes smaller than or equal to the star tracker's limiting magnitude: $V \leq V_{lim}$. The error in these observations is modeled as described in Section 3.3. These new on-board observations are also processed by a least-squares estimator and help reduce the uncertainty in the relative CubeSat-asteroid flyby trajectory.

A schematic of the behavior of asteroid ephemeris uncertainty along time is provided in Fig. 3, considering new ground-based observations prior to the CubeSat mission and collection of on-board observations. As such, uncertainty in asteroid ephemerides increases along time according to the natural dynamics of the system (Eq. (4)), unless new observations of the asteroid are available (either ground-based or on-board), in which case, ephemeris uncertainty decreases according to the quality of the observations (processed by a least-squares estimator). The timeline of ground-based and on-board observations is also summarized in Table 3.

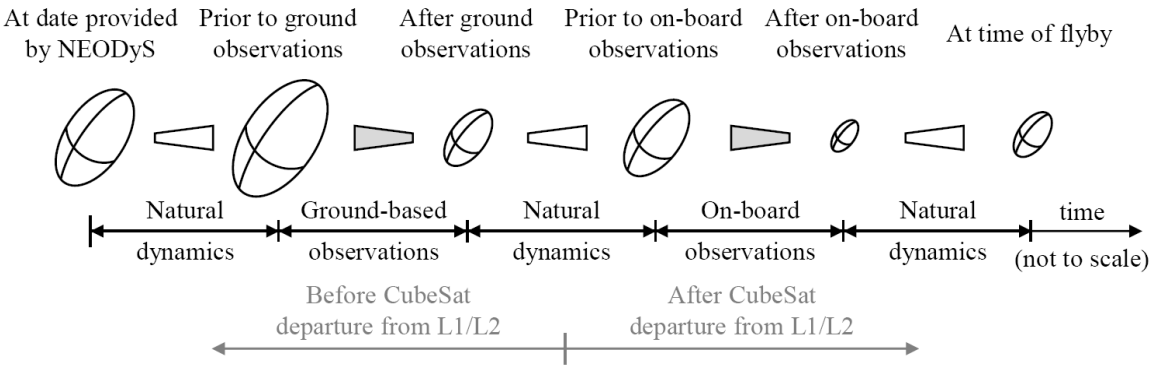

Fig. 3. Qualitative representation of asteroid ephemeris uncertainty ellipsoid prior to and along CubeSat mission (including effect of ground-based and on-board observations).

Table 3
Allocated time for ground-based and on-board navigation phases.

Type of observation		**From**	**Until**	**Every**
Ground-based observations of asteroid		Asteroid's visual magnitude from Earth below 22 ($V \leq 22$)	10 days after $V \leq 22$ from Earth	24 hours
On-board navigation, Phase 1	Observations of Sun Observations of planets	Departure from L1/L2 plus 24 hours	Asteroid's visual magnitude from CubeSat below 11 ($V \leq 11$) minus 24 hours	6 hours
On-board navigation, Phase 2	Observations of asteroid	Asteroid's visual magnitude from CubeSat below 11 ($V \leq 11$) plus 30 minutes	End of on-board navigation*	30 minutes

* On-board navigation ends 15 minutes before last trajectory correction maneuver is performed (see Section 4.2).

3.5. Error in Radiometric Observations

In the alternative scenario of a mission with some minimal ground support, radiometric observations could provide range and range rate measurements through two-way Doppler tracking [68]. Analysis in [33] identified JPL's 0.5U X-band Iris radio as a suitable deep-space communications radio for 3U and larger missions [69,70]. Iris radio is also expected to support two-way Doppler tracking with performance similar to that of regular-size missions [71]: 1 m (1σ) in range and 0.1 mm/s (1σ) in range rate [72]. These values are also assumed in the analysis of a semi-autonomous mission in Section 5.3, with only one radiometric observation per month (range and range rate). Note that radiometric observations are not considered in the fully-autonomous baseline mission scenario.

4. Autonomous Navigation and Guidance

Navigation and guidance are assumed to be performed autonomously throughout the asteroid flyby trajectory: from departure from L1/L2 until the asteroid flyby. In order to reduce the on-board computational demand, all on-board navigation and guidance algorithms propagate the estimated trajectories of the CubeSat and of the asteroid—and associated covariance matrices (STMs)—using an STM-based propagation rather than numerical propagation of their equations of motion. No computationally intensive optimization algorithms are employed in the calculation of correction maneuvers either; instead, a simple yet effective heuristic approach is proposed in this study (Section 4.2), based only on navigation covariance matrices and dynamics STMs.

The STMs employed for trajectory propagation are those associated to the nominal, reference trajectories of the CubeSat and of the asteroid, and could be calculated and stored on the CubeSat's on-board computer prior to L1/L2 departure. In such a way, propagation of the estimated trajectories (for instance, from time t_1 to t_2) can be performed simply by multiplying pre-stored state-transition matrices and estimated deviations from the nominal trajectories (Eq. (7)).

$$\boldsymbol{x}_{est}(t_2) = \boldsymbol{x}_{nom}(t_2) + \underline{\boldsymbol{\phi}}_{nom}(t_2, t_1) \cdot \left(\boldsymbol{x}_{est}(t_1) - \boldsymbol{x}_{nom}(t_1)\right) \tag{7}$$

where the subscripts est and nom stand for variables evaluated along the estimated and nominal trajectories, respectively. While the process described in Eq. (7) provides only a linear approximation of the results that would be obtained through numerical integration of the equations of motion, it also reduces the demand on on-board computational power and delivers satisfactorily accurate results (Section 5.2).

4.1. Navigation Strategy

The on-board navigation strategy consists of two phases: initially, (1) collecting observations of the Sun and visible planets after departure from L1/L2 until the asteroid becomes visible (i.e., deep-space navigation), and then, (2) collecting observations of the target asteroid until the last trajectory correction maneuver is performed (i.e., relative optical navigation). The timeline

for observations is summarized in Table 3. Throughout both navigation phases, observations are processed by a standard least-squares estimator [67].

During the deep-space navigation phase, observations are used to estimate only the heliocentric trajectory of the CubeSat. During the relative navigation phase, the heliocentric trajectories of the CubeSat and of the asteroid are simultaneously estimated instead (e.g., as in the Rosetta mission [73]). It should be noted, however, that on-board observations of the asteroid can only improve the estimation of the relative CubeSat-asteroid trajectory. Thus, alternatively, the estimation process during the second navigation phase could directly estimate the relative CubeSat-asteroid trajectory instead of both of their heliocentric trajectories.

The *a priori* estimation for the deep-space navigation phase is the CubeSat's position and velocity along its nominal trajectory at the time of departure from L1/L2, and the *a priori* covariance matrix is that described in Section 3.1. During the relative navigation phase, simultaneous estimation of the trajectories is performed by extending the estimated state vector through concatenation of the CubeSat's and asteroid's state vectors: $\boldsymbol{x}_{ext}$, and by building a 12x12 covariance matrix $\underline{\boldsymbol{P}}_{ext}$ such as that described in Eq. (8).

$$\boldsymbol{x}_{ext} = \begin{bmatrix} \boldsymbol{x}_{CubeSat} \\ \boldsymbol{x}_{asteroid} \end{bmatrix}$$
$$\underline{\boldsymbol{P}}_{ext} = \begin{bmatrix} \underline{\boldsymbol{P}}_{CubeSat} & \underline{\boldsymbol{0}}_{6x6} \\ \underline{\boldsymbol{0}}_{6x6} & \underline{\boldsymbol{P}}_{asteroid} \end{bmatrix} \tag{8}$$

where $\boldsymbol{x}_{CubeSat}$ and $\underline{\boldsymbol{P}}_{CubeSat}$ are the estimated state vector of the CubeSat and associated covariance matrix, and $\boldsymbol{x}_{asteroid}$ and $\underline{\boldsymbol{P}}_{asteroid}$ are those associated to the trajectory of the asteroid.

The resulting estimation from the deep-space navigation phase is used as *a priori* estimation of the CubeSat's trajectory in the relative navigation phase, and the nominal, reference trajectory of the asteroid is used as its *a priori* estimation. Lastly, the *a priori* covariance matrix associated to the asteroid is obtained as described in Section 3.4.

Corresponding propagations of the covariance matrices along time are performed employing Eq. (5) unless propulsive maneuvers are executed. In the presence of propulsive maneuvers, the CubeSat's covariance matrix is updated through Eq. (9) to account for maneuver execution errors [74,75]. Maneuver execution errors are introduced as process noise, $\underline{\boldsymbol{Q}}_{man}$, which is calculated as described in Section 3.2.

$$\underline{\boldsymbol{P}}_{CubeSat}(t_{man}^{+}) = \underline{\boldsymbol{P}}_{CubeSat}(t_{man}^{-}) + \underline{\boldsymbol{Q}}_{man} \tag{9}$$

where $\underline{\boldsymbol{P}}_{CubeSat}(t_{man}^{-})$ and $\underline{\boldsymbol{P}}_{CubeSat}(t_{man}^{+})$ are the navigation covariance matrices before and after the execution of an impulsive maneuver at time t_{man}.

Another relevant aspect to the deep-space navigation phase is deciding what planets should be observed and in which order. This decision is based upon the analysis in [76] which showed that most accurate estimations are obtained by observing pairs of planets that are as close as possible to the observer and whose lines of sight are closest to 90 degrees. Such a strategy will deliver the highest level of accuracy that can be obtained through observations of planets (in the order of thousands of km) through the fewest number of planet observations.

A selection factor is introduced in [76] to determine which planets should be observed (see Eq. (10)), in terms of the sum of distances from the observer to the pair of planets, r_s, and the angle between the lines of sight, θ_s.

$$\text{Selection Factor} = \sin(\theta_s)/r_s \tag{10}$$

All combinations of two visible planets are considered, and their respective selection factors are computed at each of the observation times along the deep-space navigation phase (Table 3). Pairs of planets with the highest selection factor are identified and selected for observation through the navigation camera at two consecutive observation times. Visibility of planets is determined by their visual magnitude (i.e., if smaller than V_{lim}) and shall avoid a solar exclusion angle of 40 degrees. If only one planet is visible, then that planet is observed; and if no planet is visible, then only sun sensor observations are collected. For reference, planets are generally visible along asteroid flyby trajectories more than 80% of the time, so sun sensor observations—although lower in accuracy—can support the navigation process in the remaining <20% of the time. It is also worth mentioning that the sequence of planets to be observed is determined here using the nominal trajectory of the CubeSat (not its estimated trajectory on board), and, therefore, this planet-observation sequence can be decided and stored in the CubeSat's on-board computer prior to its departure from L1/L2.

4.2. Guidance Strategy

Preliminarily analysis on the feasibility of autonomous operations for the proposed mission concept was already performed in [33]. A guidance strategy consisting of a single trajectory correction maneuver at the end of the relative navigation phase was studied. Results showed that flyby accuracies are primarily driven by the duration of this relative navigation phase: i.e., how early in advance the target asteroid is detected by the CubeSat, since this drives relative navigation accuracies. Furthermore, large ΔVs are required to correct the trajectory of the CubeSat since asteroids generally become visible only a few days before the flyby. A more effective guidance strategy is therefore required and proposed here, which is composed of more than one TCM and is able to relax the severe requirements on ΔV and limiting magnitude of the navigation camera.

The challenge that arises from a strategy with multiple TCMs is deciding how many and when TCMs should be executed, and how much ΔV should be allocated to each of them. A few factors should be considered to determine TCM execution times: (1) the later TCMs are executed, the better the estimation accuracy, (2) the sooner TCMs are executed, the lower the ΔV required to correct the trajectory, however, also, (3) the sooner TCMs are executed, the larger the inaccuracies at the time of the flyby due to propagation of maneuver execution errors.

A guidance strategy with TCMs along the deep-space navigation phase, for instance, would be able to initially reduce deviations from the nominal trajectory at a low ΔV cost. Note that only limited accuracy can be provided by these maneuvers, since no relative navigation knowledge is available yet, but they can still reduce the ΔV demand on TCMs along the relative navigation phase (and enable a later execution of TCMs). Ultimately, later TCMs improve relative navigation accuracies and resulting flyby accuracies.

Conventionally, TCMs could either be pre-scheduled or executed when the on-board navigation accuracy reaches a certain threshold (i.e., a predetermined, expected navigation performance) [4]. A timeout limit may also be included in case the expected performance is not achieved. However, pre-scheduled maneuvers and a strategy based on navigation accuracy thresholds can result in the execution of TCMs at suboptimal times, and thresholds are likely to require fine-tuning for each specific target asteroid.

Given the particularly strict ΔV limitations on CubeSat platforms, a more flexible, real-time strategy is proposed here, which is composed of two maneuvers: one during each navigation phase (see Fig. 4). The first trajectory correction maneuver, TCM_1, is timed in such a way that the second trajectory correction maneuver, TCM_2, can be executed as late as possible without exceeding ΔV budget (for maximum relative navigation accuracy). Such a strategy effectively aims to minimize the ΔV requirement on TCM_2, which is also beneficial when considering the non-instantaneity of this maneuver. Specifically, both TCMs are executed with the goal of achieving the same B-plane relative encounter position as in the nominal trajectories, and they are allocated as much ΔV as they require to fully correct the flyby relative position: i.e., no additional constraint is imposed on the magnitude of each individual TCM. The proposed strategy to autonomously select the fittest TCM execution times is described in Section 4.2.1, and advantages over more conventional approaches are discussed in Section 4.2.2.

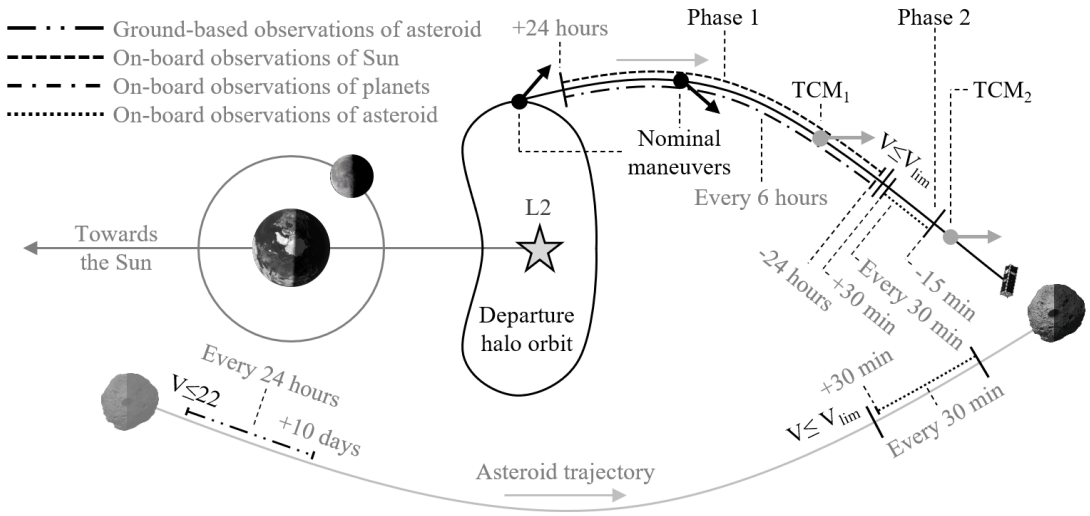

Fig. 4. Diagram of mission profile, including on-board navigation and guidance strategies.

4.2.1. Proposed Two-TCM Real-time Guidance Logic

The proposed guidance strategy considers only discrete possibilities for the times of execution of TCM_1 and TCM_2, rather than employing continuous variables. On the one hand, possible execution times for TCM_1, $\boldsymbol{t}_{\mathrm{TCM1}} = \left[t_{\mathrm{TCM1}_1}, t_{\mathrm{TCM1}_2}, \ldots, t_{\mathrm{TCM1}_n}\right]$, are considered every 5 days before the asteroid is expected to be detected. Note that the time of asteroid detection is determined based on the navigation camera's limiting magnitude (using the nominal trajectories of the CubeSat and of the asteroid). On the other hand, possible execution times for TCM_2, $\boldsymbol{t}_{\mathrm{TCM2}} = \left[t_{\mathrm{TCM2}_1}, t_{\mathrm{TCM2}_2}, \ldots, t_{\mathrm{TCM2}_m}\right]$, are considered every 12 hours after asteroid detection. Finer discretization of $\boldsymbol{t}_{\mathrm{TCM1}}$ and $\boldsymbol{t}_{\mathrm{TCM2}}$ could be implemented if desired.

Following the discussion in Section 4.2, it is expected that best flyby accuracies are achieved by executing TCM_2 as late as possible while keeping ΔV within budget: for maximum relative navigation accuracies while still fulfilling ΔV requirements. As such, at each possible t_{TCM1_i} within $\boldsymbol{t}_{\mathrm{TCM1}}$, the following steps are performed to select the TCM_1 execution time that allows for the latest possible TCM_2:

1) Compute ΔV required for TCM_1: If TCM_1 were to be executed at t_{TCM1_i}, the ΔV required to correct the B-plane position of the CubeSat is computed (inverting Eq. (7)). This calculation is performed based on the estimated CubeSat state at t_{TCM1_i} and on the nominal trajectory of the asteroid, since no relative navigation is available at this point.

2) Predict flyby covariance matrix resulting from TCM_1: Based on the estimation's covariance matrix at t_{TCM1_i}—which determines the accuracy of the ΔV computed in step (1)—the covariance matrix at the time of the flyby is predicted. Calculation of this flyby covariance matrix is performed including maneuver execution errors and the *a priori* uncertainty in asteroid ephemeris (Eq. (9) in combination with Eq. (5)). The predicted covariance matrix provides an estimate of the worst-case flyby error resulting from the hypothetical execution of TCM_1 at t_{TCM1_i}.

3) Compute ΔV required for TCM_2 depending on execution time: For all possible t_{TCM2_j} within $\boldsymbol{t}_{\mathrm{TCM2}}$, the required ΔV to correct the worst-case flyby position error predicted in step (2) is calculated (inverting Eq. (7)). In particular, only the semi-major axis of the predicted B-plane 3σ error ellipse is corrected in this analysis, as an approximation of the largest TCM_2 that would be required to correct the flyby error resulting from executing TCM_1 at t_{TCM1_i}. Note that such an approximation generally results in conservative estimations of the required ΔV for TCM_2 (further discussed in Section 4.2.2), although exceptions may arise if a particular Monte Carlo case lies near or beyond the 3σ confidence interval.

4) Compute total ΔV resulting from TCM_1 and possible TCM_2's: The ΔV requirements computed in steps (1) and (3) are added together to determine the total ΔV required for trajectory correction maneuvers depending on when TCM_2 is executed.

In summary, for each t_{TCM1_i}, steps (1–4) yield a vector of total ΔV requirements (TCM_1 plus TCM_2) corresponding to possible TCM_2 execution times t_{TCM2} (Fig. 5). From such a vector, the latest t_{TCM2_j} that still fulfills ΔV budget can be identified. If this procedure is repeated for all elements in $\boldsymbol{t}_{\mathrm{TCM1}}$, it will be observed that, initially, delaying TCM_1 also allows to delay TCM_2 as a result of improving estimation accuracy along the deep-space navigation phase (scenario A in Fig. 6); and, eventually, delaying TCM_1 requires TCM_2 to be executed earlier in order to remain within ΔV budget (scenario B in Fig. 6). The fittest solution is here identified as the TCM_1 execution time that allows for the latest TCM_2.

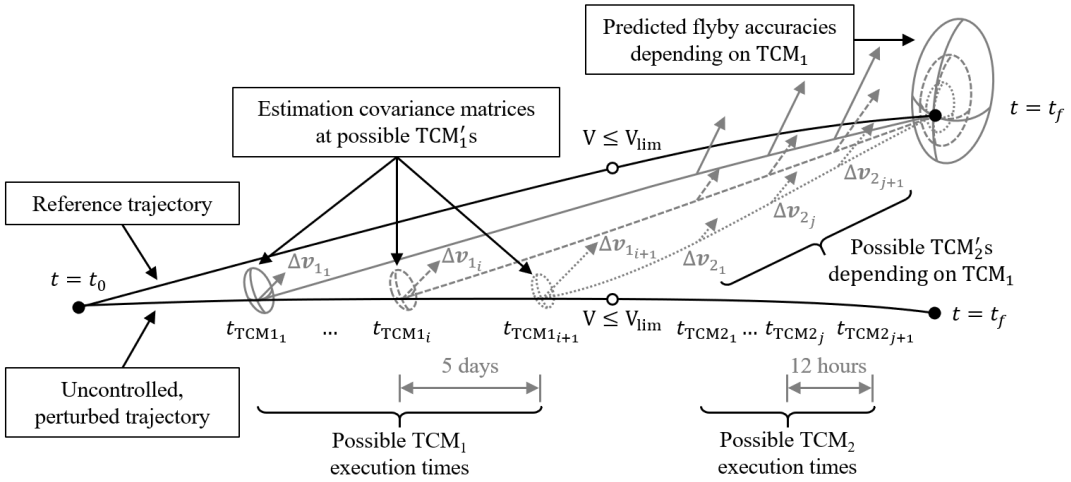

Fig. 5. Diagram of heuristic approach to determine fittest TCM_1 execution time based on estimation covariance matrices.

Note, moreover, that this real-time strategy is only required to decide whether TCM_1 should be executed at the current t_{TCM1_i}, or if it should be delayed instead. As such, at any given t_{TCM1_i}, the on-board computer is required to predict the latest possible TCM_2 only for t_{TCM1_i} and for the following execution time $t_{\mathrm{TCM1}_{i+1}}$ (see Fig. 6). On-board prediction of the latest

possible TCM_2 for $t_{TCM1_{i+1}}$, however, involves completion of steps (1–4) based only on the information available on board until t_{TCM1_i}. In order to perform this prediction, it is thus required to forecast the value of two variables at time $t_{TCM1_{i+1}}$: (a) the CubeSat state, and (b) the covariance matrix associated to the on-board navigation process.

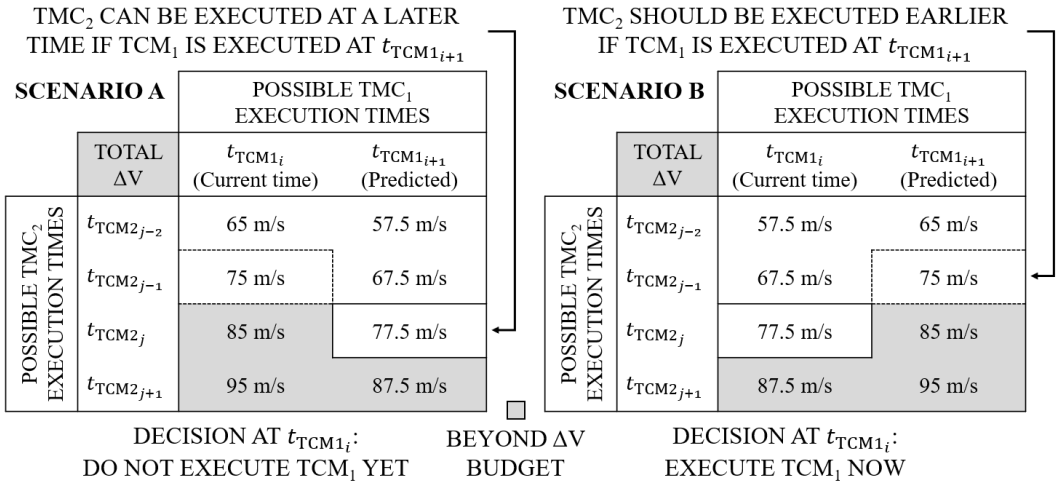

Fig. 6. Logic to determine whether TCM_1 should be executed later or at current possible execution time (ΔV budget of 80 m/s).

a) Prediction of CubeSat state: The CubeSat state at $t_{TCM1_{i+1}}$ is predicted by forward-propagating the estimated state at time t_{TCM1_i} through Eq. (7).

b) Prediction of navigation covariance matrix: Since the sequence of planets to be observed is known and can be pre-stored in the on-board computer (Section 4.1), the covariance matrix of observations to be collected between times t_{TCM1_i} and $t_{TCM1_{i+1}}$ is also known (Eq. (4)). The estimation's covariance matrix at time $t_{TCM1_{i+1}}$ can therefore be predicted based on the covariance matrix at time t_{TCM1_i} and through the typical update equation for the covariance matrix in a least-squares estimator [67], which has the form: $\underline{\boldsymbol{P}}_{new} = \left(\underline{\boldsymbol{P}}_{old}^{-1} + \sum_k \underline{\boldsymbol{T}}_{obs,k}^{T} \cdot \underline{\boldsymbol{Q}}_{obs,k}^{-1} \cdot \underline{\boldsymbol{T}}_{obs,k}\right)^{-1}$, where $\underline{\boldsymbol{Q}}_{obs,k}$ is the covariance matrix of observation k, and $\underline{\boldsymbol{T}}_{obs,k}$ is its associated observation matrix.

To recap, then, the proposed real-time heuristic will execute TCM_1 as soon as the on-board computer predicts that, if TCM_1 is delayed any further, TCM_2 should be executed earlier in order to remain within ΔV budget. On the other hand, the time of execution of TCM_2 is selected during the second navigation phase, once relative navigation knowledge is available. Similarly to TCM_1, TCM_2 is executed if, at t_{TCM2_j}, the on-board computer predicts that the ΔV budget would be exceeded if TCM_2 is executed at $t_{TCM2_{j+1}}$. Therefore, at any given t_{TCM2_j}, the on-board computer should predict the CubeSat state at $t_{TCM2_{j+1}}$ based on the estimation at t_{TCM2_j} (Eq. (7)), and compute the ΔV required to correct the relative B-plane flyby

position if TCM_2 is executed at $t_{TCM2_{j+1}}$ (inverting Eq. (7)). If the ΔV requirement at $t_{TCM2_{j+1}}$ is larger than the remaining ΔV, then TCM_2 is executed at the current TCM_2 execution time t_{TCM2_j} (scenario B in Fig. 7).

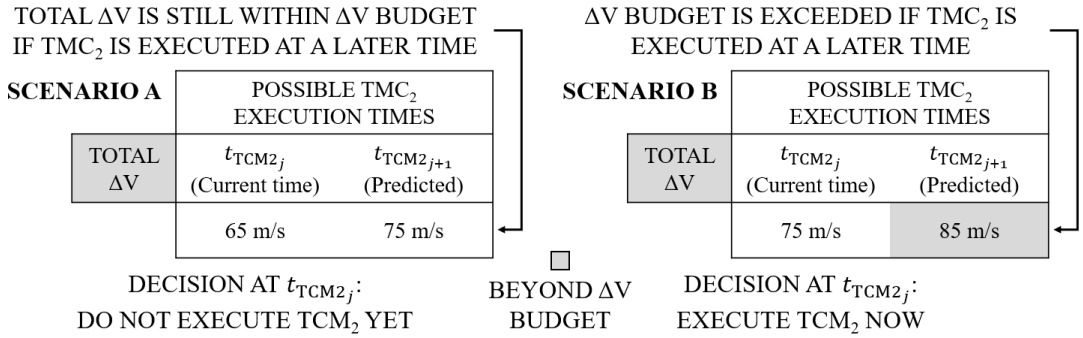

Fig. 7. Logic to determine whether TCM_2 should be executed later or at current possible execution time (ΔV budget of 80 m/s).

Note that, when considering the non-instantaneity of TCM_2, the proposed strategy to time TCM_1 still provides a valid approach, since it aims to reduce the ΔV requirement on TCM_2 (which then reduces maneuver execution times). In order to time TCM_2, however, the proposed strategy may need to consider an additional "if" condition: e.g., "execute TCM_2 if the ΔV requirement at $t_{TCM2_{j+1}}$ exceeds ΔV budget, or if the time required to execute TCM_2 starting at $t_{TCM2_{j+1}}$ is longer than the time until the flyby." For a 6U platform, this second condition may only be fulfilled within 6 hours from the flyby (in the extreme scenario where the full 80 m/s are required for TCM_2), and up to 1.5 days before the flyby for a 3U platform. Future work may need to evaluate performance differences between an impulsive model and a higher-fidelity thrusting model composed of finite-duration, continuous thrust arcs (most relevant to a 3U mission).

As a final comment, it should be highlighted that the two maneuvers along the nominal trajectory—those computed in [32] and illustrated in Fig. 4—are executed as per design (plus maneuver execution errors), and they are not recalculated or redesigned by the on-board computer. The justification for this is twofold: (1) navigation accuracy at the time of the second nominal maneuver is generally not good enough to improve final flyby accuracies, and (2) propagation of maneuver execution errors from the time of the second nominal maneuver until the asteroid encounter induce large flyby inaccuracies. No improvements in flyby accuracies can therefore be obtained even if the nominal maneuvers are recalculated based on the on-board estimation.

4.2.2. Advantages of Proposed Real-time Guidance Logic

The proposed strategy is here compared to more conventional approaches to time TCMs: navigation accuracy thresholds and pre-scheduled maneuvers. As an initial step in the discussion, results for target asteroid 2017 XC62 employing the proposed strategy are illustrated in Fig. 8 and Fig. 9 (refer to Section 5.2 for a more elaborated discussion on these results). Illustrated in Fig. 8 is the selected time of execution of TCM_1 for a total of 10,000 Monte Carlo runs, and Fig. 9 illustrates the corresponding

on-board navigation accuracy at the time of execution of TCM_1 (represented by the largest semi-axis of the navigation covariance matrix). Note that the columns with a value of zero in Fig. 9 are due to the discretization of possible TCM_1 execution times (which results in discrete values of possible navigation accuracies), and columns with a zero value in Fig. 8 simply correspond to possible execution times that are not selected by the proposed strategy.

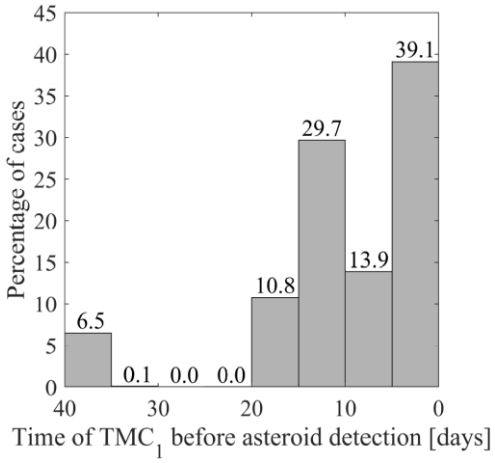

Fig. 8. Histogram of time of execution of TCM_1 in Monte Carlo runs (asteroid 2017 XC62).

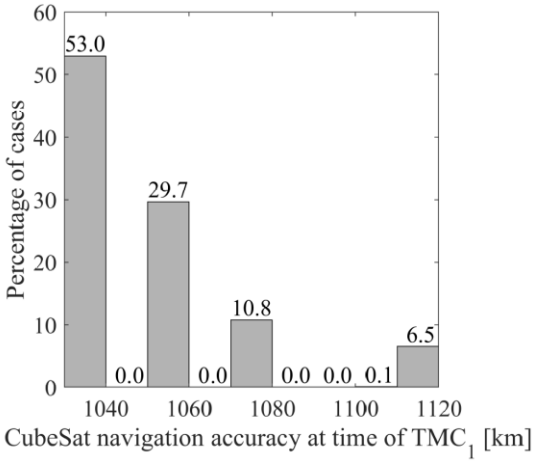

Fig. 9. Histogram of CubeSat navigation accuracy at time of TCM_1 in Monte Carlo runs (asteroid 2017 XC62).

It is observed that selected TCM_1 execution times widely vary amongst different Monte Carlo cases, whereas a strategy based on pre-scheduled maneuvers would be limited to a single execution time for all cases. Similarly, TCM_1 is executed at a range of different on-board navigation accuracies, which could not be featured by a strategy based on a single navigation accuracy threshold.

One of the key aspects to select the time of execution of TCM_1 is providing a conservative estimate of the largest ΔV that would be required for TCM_2: so that TCM_1 allows for the latest possible TCM_2 while not exceeding ΔV budget. Such a worst-case estimate is computed in this study as the ΔV required to correct the semi-major axis of the predicted 3σ B-plane error ellipse after executing TCM_1 (Section 4.2.1), although alternative solutions could be implemented. Nevertheless, and as illustrated in Fig. 10, such an approach does generally result in conservative estimations of the largest ΔV that would be required for TCM_2.

Represented in Fig. 10 are the magnitudes of the worst-case TCM_2 maneuvers estimated at TCM_1 execution time (y-axis), versus the magnitude of the actually-executed TCM_2 maneuvers (x-axis), corresponding to various TCM_2 execution times and for the same flyby scenario as in Fig. 8 and Fig. 9. Illustrated in Fig. 11 is then the distribution of actually-executed TCM_2 ΔV magnitudes. It is firstly observed in Fig. 10 that all data points are above the line of slope one, which indicates that, in this flyby scenario, none of the executed TCM_2 maneuvers exceeds the conservative TCM_2 estimation. In fact, TCM_2 maneuvers are never executed earlier than the worst-case TCM_2 execution times estimated at TCM_1 execution time. Secondly, it is seen that,

for a given TCM_2 execution time (e.g., 6 hours before flyby), only discrete values of estimated TCM_2 magnitudes are recorded, which correspond to the different times at which these worst-case TCM_2 maneuvers were estimated: i.e., to the discrete values of possible TCM_1 execution times (Section 4.2.1). More specifically, later estimation times result in smaller estimated TCM_2 maneuvers, since the navigation accuracy at later TCM_1 execution times is improved and the time for propagation of maneuver execution errors is reduced. Thirdly, it can be observed that later TCM_2 execution times result in larger worst-case TCM_2 magnitudes (which may be up to hundreds of m/s), since shorter amounts of time are available to correct the trajectory; whereas the actually-executed maneuvers are always below 40 m/s. Contrariwise, it is shown in Fig. 11 that later TCM_2 execution times, which are also shown less common, are actually associated to Monte Carlo cases that require smaller TCM_2 maneuvers.

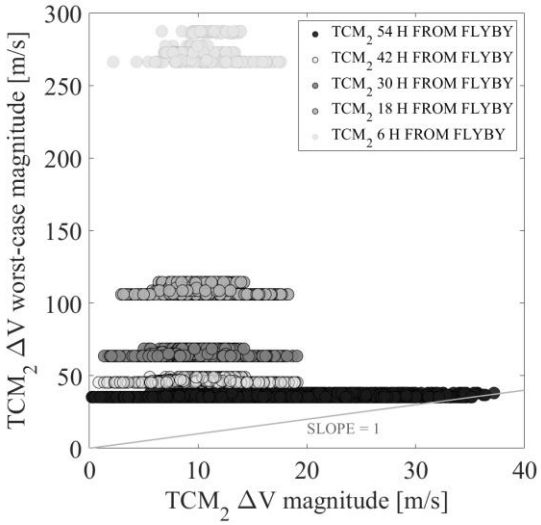

Fig. 10. Estimated worst-case TCM_2 ΔV magnitudes vs actually-executed TCM_2 ΔV magnitudes (asteroid 2017 XC62).

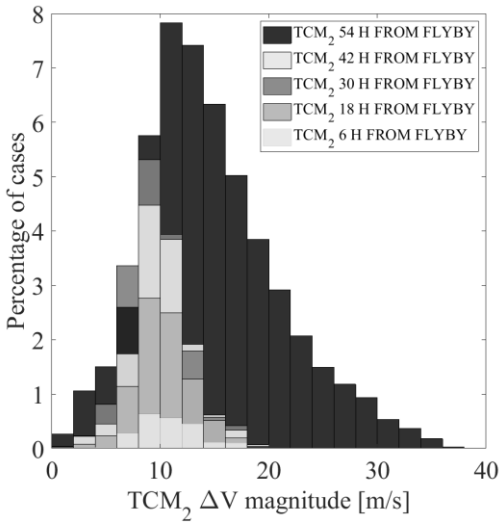

Fig. 11. Histogram of actually-executed TCM_2 ΔV magnitudes (asteroid 2017 XC62, and 2-m/s discretization bins).

Performance advantages of the proposed guidance strategy are also illustrated by Table 4 and Fig. 12. Table 4 shows the number of asteroids for which flyby accuracies better than ±100 km (3σ) are possible for three different scenarios: if (1) TCM execution times are selected according to the proposed guidance strategy, and if (2) TCM_1 or (3) TCM_2 are delayed with respect to those selected TCM execution times. If TCMs are timed such that TCM_1 allows for the latest possible TCM_2 within ΔV budget, flyby accuracies better than ±100 km (3σ) are possible for up to 11 asteroids from L1 and L2. If TCM_1 is delayed 5 days in every Monte Carlo simulation, then flyby accuracies better than ±100 km (3σ) are possible for only 9 of the earlier 11 asteroids; and if TCM_2 is delayed for 12 hours, this number is reduced down to 4 of the 11 asteroids. Table 4 therefore shows that flyby accuracies are highly sensitive to the time of execution of TCMs, especially if the maneuver during the relative navigation phase, TCM_2, is executed when the required ΔV already exceeds ΔV budget. It is further argued that if TCM_2 is executed any earlier, flyby accuracies would also worsen since lower levels of relative navigation accuracy would be available to the on-board computer.

Table 4
Number of asteroids for which flyby accuracies better than ±100 km (3σ) are possible, depending on TCM execution time.

	TCMs timed according to proposed guidance strategy	**TCM_1 delayed 5 days in every Monte Carlo run**	**TCM_2 delayed 12 hours in every Monte Carlo run**
From L1	6	5	3
From L2	5	4	1
Total	11	9	4

Furthermore, Fig. 12 considers an alternative scenario in which TCM_1 is executed according to a predetermined navigation accuracy threshold, and TCM_2 is timed as in the proposed strategy (before exceeding ΔV budget). Selection of a navigation accuracy threshold requires fine-tuning for each specific asteroid, and, for the purpose of this discussion, a threshold of 1060 km (3σ) is established for asteroid 2017 XC62 (second most common navigation accuracy in Fig. 9). Imposing such a threshold is also equivalent to pre-scheduling TCM_1 approximately 10 days before asteroid detection in all Monte Carlo cases, which effectively brings TCM_1 forward for the 53.0% of cases whose TCM_1 was executed less than 10 days before asteroid detection (most common navigation accuracy in Fig. 9), and delays the 17.3% of cases that were executed earlier.

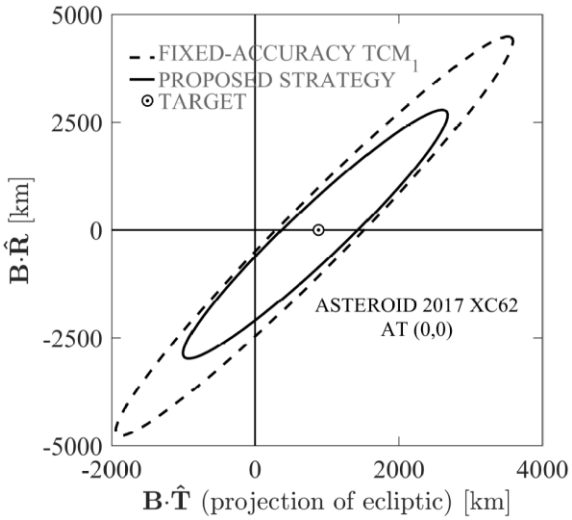

Fig. 12. B-plane 3σ error ellipses for fixed-navigation-accuracy TCM_1 strategy and proposed strategy (asteroid 2017 XC62).

The performance of this alternative scenario is compared to the proposed guidance strategy in Fig. 12 by means of the resulting B-plane error ellipses. It is observed that executing TCM_1 based on a predetermined threshold delivers an error ellipse approximately 1.5 times larger than the proposed guidance strategy. This further evidences the need for a flexible real-time guidance strategy that is not based on pre-scheduled maneuvers or fixed navigation accuracy thresholds. Such a flexible strategy is proposed in this study, which times TCMs based on real-time on-board knowledge of navigation accuracy and deviations from the nominal trajectories. Such an approach does not require fine-tuning of parametric thresholds for each target asteroid either, and TCMs are calculated and timed employing only state-transition matrices associated to the dynamics and covariance matrices associated to the navigation process—which also avoids numerical integration of equations of motion and complex optimization methods.

As discussed in Section 5.2, the proposed strategy is also able to relax the high demand on the navigation camera's limiting magnitude imposed in [33]: i.e., better flyby accuracies for a larger number of asteroids with V_{lim}=11 instead of V_{lim}=15. Uncertainties in asteroid ephemerides are also considered here, and observations of visible planets are introduced to improve navigation accuracies prior to asteroid detection. Discussion on the results obtained through the proposed guidance strategy can be found in Section 5.2 (for the baseline mission scenario), and the effectiveness of the strategy for alternative system specifications can be found in Section 5.3.

5. Analysis and Discussion

A Monte Carlo analysis is performed to characterize the flyby accuracies that can be achieved through the autonomous navigation and guidance strategy described in Section 4. However, as an initial step, it is required to assess the accuracy in asteroid ephemeris that will be available to the CubeSat as it departs from L1/L2, which can then provide insight into how ephemeris quality affects final flyby accuracies.

5.1. Ground-based Asteroid Observation Campaign

As described in Section 3.4, whenever the target asteroid is observable from Earth prior to L1/L2 departure (V≤22), a ground-based observation campaign is simulated and asteroid ephemerides are updated. Adding more recent observations to the ephemeris estimation increases the observed arc length of the asteroid's orbit (time between first and last ground-based observations), and, as a result, the uncertainty in asteroid ephemeris decreases. This decreasing behavior in ephemeris uncertainty was analyzed in [66] and modeled through a piecewise linear function in a logarithmic scale (Fig. 13).

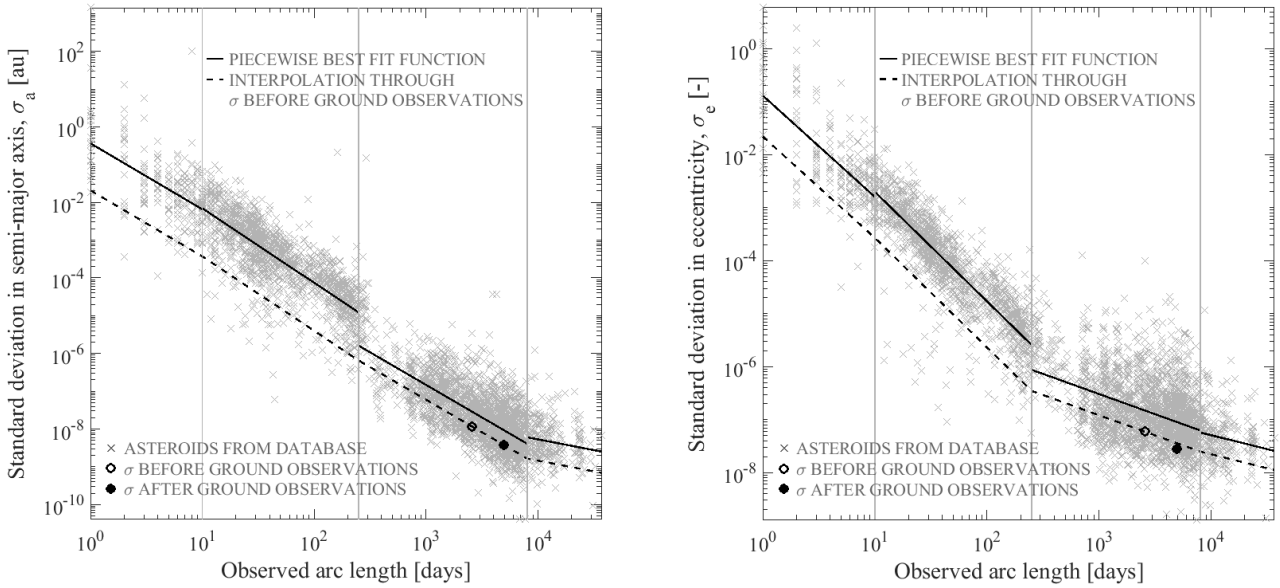

Fig. 13. Keplerian element uncertainty (left: semi-major axis, right: eccentricity) for asteroid 2005 WD before and after collecting ground-based observations.

In this study, new ground-based observations are modeled and processed as described in Section 3.4, and results are compared to the expected piecewise behavior for validation. As an example, illustrated in Fig. 13 are the resulting uncertainties in Keplerian semi-major axis (left) and eccentricity (right) at the time of the flyby, before and after the simulated observation campaign (asteroid 2005 WD). It is observed that the improvement in uncertainties is in accordance with the best-fit piecewise function. Note that the "background" data in Fig. 13 only include asteroids with similar characteristics to the target asteroids described in Section 2: asteroids larger than 100 meters in diameter that fly close to Earth (within 0.1 au) between years 2019 and 2030.

Table 5 then summarizes the results from the simulated ground-based observation campaigns for all asteroids analyzed in the baseline mission scenario: those reachable with less than 75 m/s and visible for more than 6 hours with V_{lim}=11. Observed arc lengths before and after collecting ground-based observations are summarized, as well as the corresponding ephemeris uncertainties at the time of the flyby (represented by the largest semi-axis of their 3σ covariance matrix). It is observed that significant improvements in uncertainty are obtained for asteroids with low arc lengths prior to new ground observations, for which uncertainties above 10,000 km are reduced below 1000 km: e.g., asteroids 2017 XC62, 2014 HK129, and 2018 CC14. This improvement is less prominent, however, if <1000-km uncertainties were already available: e.g., asteroids 2005 WD, 2008 TZ3, 1998 ST27, etc.

It can thus be concluded that a ground-based observation campaign is essential for asteroids with large ephemeris uncertainties (>10,000 km), since an observation campaign can significantly decrease their uncertainty. Otherwise, uncertainty improvements may not be substantial and an observation campaign prior to the mission may not be strictly necessary.

5.2. Analysis of Baseline Mission Scenario

This section summarizes the results from 10,000 Monte Carlo simulations employing the two-TCM guidance strategy described in Section 4.2.1 (Table 6). These results are also compared to three other guidance scenarios: (1) one-TCM scenario: only one TCM is executed during the relative navigation phase (such as that considered in [33]), (2) no-TCM scenario: no TCMs are performed, which illustrates the deviations produced only by initial state uncertainties and execution errors in the nominal propulsive maneuvers, and (3) no relative navigation scenario: only one TCM is executed at the end of the deep-space navigation phase, which illustrates the results of a mission without CubeSat-asteroid relative navigation phase (observations of the Sun and planets only). In the one-TCM scenario, selection of the TCM execution time is performed following the same procedure as for TCM_2 in the two-TCM guidance strategy (Section 4.2.1, Fig. 7): predicting the ΔV cost at the next possible TCM execution time until that cost exceeds the available ΔV budget.

Table 5
Nominal flyby characteristics and effect of new ground-based observations.

Asteroid	From	Nominal trajectory characteristics [32]		Visible days by CubeSat	Improvement through ground-based astrometric observations	
		Time of flight (days)	ΔV range from L1/L2 (m/s)		Observed arc length (days)	3σ uncertainty at time of flyby (km)
2005 WD	L2	141.7↔150.0	59.1↔69.2	0.8	2565↔4956	95.9↔81.9
2015 BK509*,†		150.0	47.2	0.8	27	3487243.0
2008 TZ3		129.7↔149.9	42.5↔56.9	7.1	3632↔4068	37.8↔37.6
2004 UE*		150.0↔137.5	39.1↔54.3	0.4	178	2055922.4
2017 XC62		150.0↔141.8	26.0↔60.5	2.4	176↔1348	119981.4↔498.1
1989 JA*		142.2↔140.0	36.7↔66.3	0.4	10889	339.7
1998 ST27		138.1↔109.2	23.6↔61.3	0.3	7309↔8427	27.0↔25.0
2008 DG5†		138.0	32.8	2.6	6494↔7945	177.3↔172.4
1997 NC1		140.4↔81.0	15.6↔68.2	0.6	7681↔10234	248.5↔223.3
2012 EY11		150.0↔149.9	68.2↔73.3	12.4	5902↔9513	359.6↔277.1
2001 SQ3		140.7↔124.5	38.4↔68.3	0.6	4518↔7730	282.3↔276.6
2001 WN5‡		150.0↔115.5	44.1↔65.0	3.8	8463↔11325	230.2↔220.6
2011 LJ19*,†		150.0	64.0	0.4	147	3297518.7
2004 OB†		149.6	36.4	1.5	5447↔8745	240.9↔222.6
2004 MN4‡		140.2↔55.9	5.7↔57.6	2.5	3946↔9009	14.6↔14.5
2001 FO32	L1	150.0↔78.1	30.5↔62.8	2.2	5009↔7216	840.5↔595.2
2016 AJ193*		138.9↔150.0	42.4↔64.7	0.3	111	641531.0
2008 AG33		150.0↔150.0	16.9↔60.9	0.4	4298↔6628	492.0↔429.6
2014 HK129†		150.0	47.3	18.4	528↔3004	35197.1↔789.9
2010 XC15*,†		141.2	26.7	0.6	2549	484.7
2018 CC14†		141.6	68.5	0.6	101↔2094	3016405.9↔313.9
2001 WN5‡		33.3↔149.9	4.4↔40.3	1.0	8463↔8700	230.1↔168.6
2011 LJ19*		117.4↔95.6	15.9↔54.0	0.5	147	3324623.3
2009 BL71		150.0↔110.8	20.3↔50.3	0.9	3716↔6961	174.3↔141.6
2004 MN4‡		125.8↔33.3	20.9↔50.7	7.3	3946↔9121	244.6↔222.7

* Asteroid ephemerides cannot be improved since they are not observable from Earth prior to L1/L2 departure.
† Reachable with <75 m/s from only one of the nine departure points along the halo orbit considered in [32].
‡ Asteroid 2001 WN5 can be reached from L1 and L2. Ephemeris uncertainties are larger for a flyby from L2 as a consequence of the asteroid's close encounter with Earth. Same applies to asteroid 2004 MN4 (Apophis) from L1.

Table 6 compares the performance of these four guidance scenarios in terms of achievable flyby accuracies (represented by the semi-major axis of B-plane 3σ error ellipses). Ranges of values in Table 6 correspond to the best- and worst-case scenarios in terms of available ΔV for TCMs [32]: (1) departure point from L1/L2 with smallest ΔV requirement below 75 m/s, and (2) departure point from L1/L2 with largest ΔV requirement below 75 m/s. Also summarized in Table 6 is the relative estimation error at the time of execution of TCM_2 for the two-TCM strategy.

As an example of the results in Table 6, Fig. 14 illustrates the resulting B-plane 3σ error ellipses from all four guidance strategies: for asteroid 2017 XC62 (19.5 m/s available for TCMs). It is observed that flyby errors in the order of tens of thousands of kilometers would be obtained if no TCMs were performed. Slightly smaller but still unreasonably large errors would be obtained if no relative optical navigation is available. Notably, it is observed that the two-TCM guidance strategy introduced in this study delivers flyby accuracies approximately one order of magnitude better than a one-TCM strategy.

Table 6
Comparison of B-plane flyby accuracies for various guidance strategies.

Asteroid	B-plane 3σ flyby accuracies (km)				B-plane 3σ relative estimation error at time of TCM_2 (km)
	Two-TCM strategy	One-TCM strategy	No-TCM strategy	No relative navigation	
2005 WD	37084↔38500	44053↔41860	51460↔45831	44071↔41861	2601↔715
2015 BK509	$3.3\cdot10^6$	$3.3\cdot10^6$	$3.3\cdot10^6$	$3.3\cdot10^6$	$1.4\cdot10^8$
2008 TZ3	14↔25	239↔6044	20147↔29233	2326↔6405	13↔23
2004 UE	$1.5\cdot10^6$↔$1.5\cdot10^6$	$1.5\cdot10^6$↔$1.5\cdot10^6$	$1.5\cdot10^6$↔$1.5\cdot10^6$	$1.5\cdot10^6$↔$1.5\cdot10^6$	$1.0\cdot10^6$↔$1.4\cdot10^6$
2017 XC62	21↔3369	13606↔24944	40308↔36773	14204↔25140	9↔59
1989 JA	9116↔18730	18260↔27100	27907↔30577	18463↔27115	2404↔6643
1998 ST27	4765↔19562	17265↔20647	27808↔24604	17318↔20661	2213↔1819
2008 DG5	814	5705	27118	7097	36
1997 NC1	2625↔6819	18528↔10407	33074↔13019	18763↔10491	23↔598
2012 EY11	2148↔27491	16546↔27503	41116↔43328	16552↔27585	146↔603
2001 SQ3	3996↔22876	22107↔31808	33763↔35438	22136↔31811	1465↔2551
2001 WN5	25↔40	713↔47	11650↔3091	2983↔2290	23↔39
2011 LJ19	$1.6\cdot10^6$	$1.6\cdot10^6$	$1.6\cdot10^6$	$1.6\cdot10^6$	$3.1\cdot10^7$
2004 OB	83	5541	20424	5567	14
2004 MN4	4↔7	11465↔15	40893↔2667	11465↔163	3↔6
2001 FO32	532↔26	46842↔1514	69923↔8305	46844↔1600	122↔25
2016 AJ193	480277↔489144	481663↔491780	481954↔492095	481746↔491784	128↔186417
2008 AG33	18↔6577	57165↔63672	71936↔68300	57165↔63672	5↔469
2014 HK129	5	86	21658	719	5
2010 XC15	149	54344	68799	54344	91
2018 CC14	184	30243	33938	30243	81
2001 WN5	4↔4	4↔2670	445↔12145	83↔2672	4↔4
2011 LJ19	$1.6\cdot10^6$↔$1.5\cdot10^6$	$1.6\cdot10^6$↔$1.5\cdot10^6$	$1.6\cdot10^6$↔$1.5\cdot10^6$	$1.6\cdot10^6$↔$1.5\cdot10^6$	$1.1\cdot10^8$↔$2.4\cdot10^7$
2009 BL71	3↔4	39018↔10767	56859↔20225	39018↔10769	3↔3
2004 MN4	3↔3	35↔7	8719↔1308	334↔233	2↔3

Performance improvements from a one-TCM to a two-TCM guidance strategy can also be observed in Fig. 15, which illustrates the distribution of distances from actual B-plane positions to the target B-plane position (i.e., the target illustrated in Fig. 14). Notice that results in Fig. 15 resemble the shape of half-normal distributions, but their statistical measures (e.g., skewness and external kurtosis) differ from those of half-normal distributions (with skewness of 0.995 and external kurtosis of 0.869). More specifically, higher levels of skewness are shown by the results from a one- and two-TCM guidance strategies: 1.701 and 2.261, respectively, which indicate a higher concentration of cases near zero distance (more so for the two-TCM strategy); and higher levels of external kurtosis: 3.357 and 5.503, indicate that the distributions approach a probability of zero at a slower rate than half-normal distributions. Nonetheless, there is an agreement better than 5% between the 99.7th percentiles in Fig. 15 and their corresponding 3σ confidence intervals. As such, the 3σ representation employed throughout this paper to describe flyby accuracies provides a sensible measure of 99.7th percentiles (as it is characteristic of normally-distributed data), even though Monte Carlo cases may not strictly follow normal distributions.

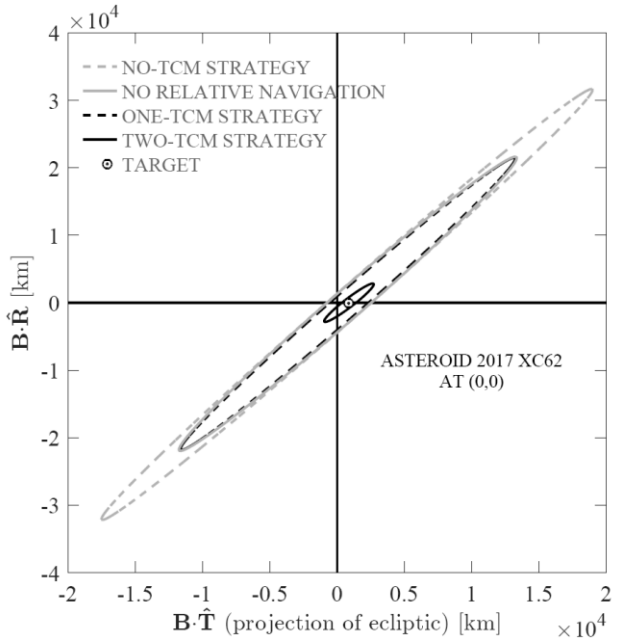

Fig. 14. B-plane 3σ error ellipses for asteroid 2017 XC62 depending on guidance strategy.

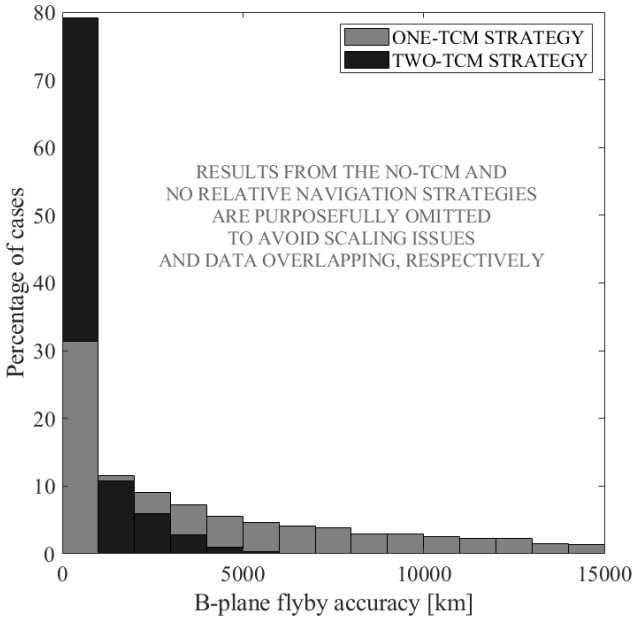

Fig. 15. Histogram of B-plane flyby accuracies for asteroid 2017 XC62 depending on guidance strategy.

The importance of the relative navigation phase is also evidenced by Fig. 16, which illustrates the evolution of the relative estimation error of the CubeSat-asteroid flyby position. It is observed how the estimation error is reduced by approximately one order of magnitude when the first observations of the asteroid are collected (i.e., $V \leq V_{lim}$).

Several more observations can be made from the results in Table 6, together with the time of flight, ΔV, and visibility information provided in Table 5; these are:

1) The two-TCM guidance strategy introduced here provides results approximately one order of magnitude better than the one-TCM strategy considered in [33]: e.g., for asteroid 2004 OB, flyby accuracies below 100 km (3σ) can be obtained through the two-TCM strategy, whereas accuracies worse than 1000 km are obtained through a one-TCM strategy.

2) Shorter transfer trajectories result in better flyby accuracies since the time for propagation of uncertainties is reduced (i.e., uncertainty in initial state and in the execution of nominal maneuvers), and so TCMs can be executed at a later time (with better navigation accuracies): e.g., better flyby accuracies are obtained for asteroid 2001 FO32 along the 78.1-day flyby trajectory despite having a larger nominal ΔV requirement (62.8 m/s) than the 150-day trajectory (30.5 m/s). The effect of uncertainty propagation time is also observed in the no-TCM results, which are significantly better for the 78.1-day trajectory. Further note that worse thruster or ADCS accuracies than those considered in Table 2 would have a similar effect to increasing time of flight.

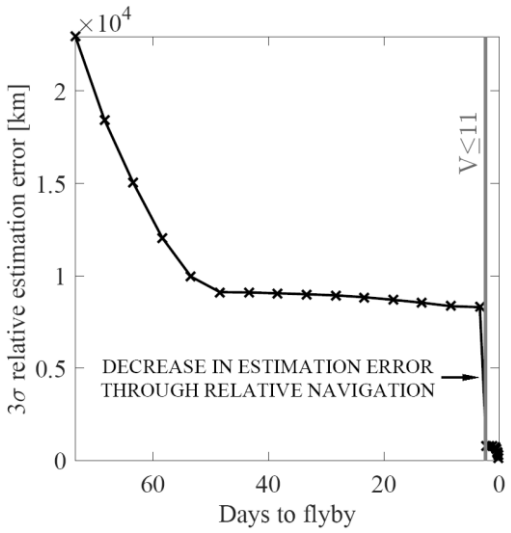

Fig. 16. Evolution of relative estimation error for asteroid 2017 XC62 as a function of time.

3) Large uncertainties in asteroid ephemeris prior to L1/L2 departure result in poor flyby accuracies: e.g., worst flyby accuracies are obtained for asteroids 2015 BK509, 2004 UE, 2011 LJ19 and 2016 AJ193, whose *a priori* ephemeris uncertainties are larger than 100,000 km. This is due to the unavailability of sufficient ΔV to correct, after asteroid detection, such large discrepancies between the *a priori* estimate and the actual position of the asteroid at the time of the flyby.

4) Early detection of the asteroid is essential to reduce estimation errors, and, effectively, to improve the resulting flyby accuracies: e.g., asteroid 1998 ST27 is detected only 0.3 days before the flyby which results in estimation and flyby accuracies one order of magnitude worse than those of asteroid 2017 XC62, which is observed for 2.4 days and has comparable nominal ΔV requirements.

5) Lower nominal ΔV requirements from L1/L2 result in better flyby accuracies since a larger ΔV is available for TCMs, and, consequently, allows TCMs to be executed at a later time: e.g., better estimation errors and flyby accuracies are obtained for asteroid 2017 XC62 along the 26.0-m/s flyby trajectory than along the 60.5-m/s trajectory, despite having a longer duration (150 days) and larger no-TCM flyby error.

It is thus seen that flyby accuracies well below 100 km (3σ) can be achieved autonomously if the two-TCM strategy presented in Section 4.2.1 is employed. In terms of system requirements, the proposed strategy allows for better flyby accuracies for a given ΔV budget than a one-TCM strategy, and it allows for a smaller limiting magnitude of the navigation camera. Additionally, navigation and guidance algorithms can propagate trajectories and compute velocity corrections employing only pre-stored state-transition matrices, which contributes to reducing the computational demand on board CubeSats.

Even though the proposed two-TCM strategy provides promising flyby accuracies even on 3U/6U platforms (80 m/s of ΔV), proper flyby accuracies can only be achieved if a suitable combination of (a) asteroid visibility time, (b) remaining ΔV for TCMs, (c) *a priori* asteroid ephemeris uncertainty, and (d) short transfer to asteroid is available. For reference, flyby accuracies below 100 km (3σ) can only be achieved for 11 out of the 25 analyzed asteroids (V_{lim}=11). In order to improve the number of asteroids with acceptable flyby accuracies, mission requirements would need to be relaxed either by increasing the size and capability of the spacecraft (Section 5.3), or by including radiometric observations for navigation (thus reducing autonomy levels of the mission—see Section 5.4).

5.3. Extended Analysis on System Performance

Asteroid visibility and ΔV budget are identified as two of the main driving factors for autonomous missions. However, improving ΔV capability or navigation camera performance would likely require a CubeSat larger than 3 units. For instance, VACCO's 3U Green Propulsion System [77] could provide 275 m/s on a 6U CubeSat (12 kg) and allocate a larger ΔV for TCMs and to reach a larger number of asteroids. It is argued that higher limiting visual magnitudes could already be achieved by the star tracker considered in Table 2 without further technological developments (e.g., V_{lim}=15 through 20-second exposure times and additional computation effort [35]). Note also that 20-second exposure times may still be compatible with the 0.03-deg CCD pixels of the considered star tracker [51], and with the jitter stability of BCT's XACT unit: <0.02-deg (10 s^{-1}) 3σ [50]. Nevertheless, a bigger navigation camera with larger aperture or focal length could also reduce exposure times and observation errors.

In an effort to provide some insight into how system specifications affect flyby accuracies, Monte Carlo simulations are also carried out for cases in which the navigation camera's limiting magnitude is V_{lim}=7, V_{lim}=9, V_{lim}=13 and V_{lim}=15 (instead of the baseline V_{lim}=11), and for cases in which the total ΔV budget is 90 m/s and 100 m/s (instead of 80 m/s). These increments in the ΔV budget ensure that at least 15 m/s and 25 m/s of ΔV are available for TCMs, even for asteroids whose L1/L2 ΔV requirements are close to 75 m/s. Limiting visual magnitudes below 11 exemplify the capabilities of ADCS units currently on the market through sub-second exposure times, and limiting magnitudes above 11 represent the capabilities of bigger navigation cameras or of 10–20-second exposure times.

Monte Carlo simulations with these alternative system specifications are performed, modifying only one system parameter at a time (indicated in Table 7) while others remain the same as in the baseline mission scenario (Table 2), and employing the two-TCM guidance strategy presented in Section 4.2.1. Out of the 36 reachable asteroids identified in [32], all asteroids observable for more than 6 hours with limiting visual magnitude V_{lim}=15 are analyzed here (a total of 29 of them), and Monte Carlo simulations are performed for the same two cases described in Section 5.2: best and worst cases in terms of available ΔV

Table 7
Feasibility of accurate asteroid flybys (better than ±100 km (3σ)) depending on system performance.

Asteroid	From	Limiting visual magnitude					ΔV budget	
		V_{lim}=7	V_{lim}=9	V_{lim}=11	V_{lim}=13	V_{lim}=15	90 m/s	100 m/s
2005 WD	L2	Not vis.						
2015 BK509		Large *a priori* ephemeris uncertainty (>100,000 km)						
2008 TZ3			Min.	All	All	All	All	All
2004 UE		Large *a priori* ephemeris uncertainty (>100,000 km)						
2017 XC62				Min.	Min.	All	Min.	Min.
1989 JA		Not vis.	Not vis.					
1998 ST27		Not vis.	Not vis.					
2008 DG5					All	All	All	All
1997 NC1		Not vis.	Not vis.			Min.		
2012 EY11					Min.	Min.	Min.	All
2001 SQ3		Not vis.	Not vis.			Min.		
2001 WN5				All	All	All	All	All
2011 LJ19		Large *a priori* ephemeris uncertainty (>100,000 km)						
2004 OB		Not vis.		All	All	All	All	All
2004 MN4		Min.	All	All	All	All	All	All
2010 PK9		Not vis.	Not vis.	Not vis.			Not vis.	Not vis.
2015 JD1		Not vis.	Not vis.	Not vis.			Not vis.	Not vis.
1999 AN10		Not vis.	Not vis.	Not vis.	Not vis.		Not vis.	Not vis.
2001 FO32	L1		Max.	Max.	All	All	All	All
2016 AJ193		Large *a priori* ephemeris uncertainty (>100,000 km)						
2008 AG33		Not vis.	Not vis.	Min.	Min.	Min.	Min.	Min.
2014 HK129		All	All	All	All	All	All	All
2010 XC15		Not vis.	Not vis.			All	All	All
2018 CC14		Not vis.			All	All	All	All
2001 WN5		Not vis.	All	All	All	All	All	All
2011 LJ19		Large *a priori* ephemeris uncertainty (>100,000 km)						
2009 BL71		Not vis.	All	All	All	All	All	All
2004 MN4		Min.	Min.	All	All	All	All	All
2010 JG		Not vis.	Not vis.	Not vis.			Not vis.	Not vis.
2008 GO20		Not vis.	Not vis.	Not vis.			Not vis.	Not vis.
2006 YT13		Not vis.	Not vis.	Not vis.	All	All	Not vis.	Not vis.
2007 ML24		Not vis.	Not vis.	Not vis.	Min.	All	Not vis.	Not vis.

All: Accurate flyby is feasible from L1/L2 departure points with minimum and maximum nominal ΔV requirements.
Min./Max.: Accurate flyby is only feasible from L1/L2 departure point with minimum/maximum nominal ΔV requirement.
Blank if accurate flyby is not feasible neither from L1/L2 departure point with min. nor max. nominal ΔV requirement.
Not vis.: Asteroid is not visible for more than 6 hours before the flyby with associated limiting visual magnitude.

for TCMs (L1/L2 departure points with minimum and maximum nominal ΔV requirements below 75 m/s out of the nine departure points considered in [32]).

Table 7 summarizes results from these Monte Carlo simulations (1000 runs) and indicates whether accurate flybys are possible through the baseline mission scenario, or through any of the alternative system specifications—where "accurate" flybys are here defined as those with B-plane accuracies better than ±100 km (3σ). It is worth mentioning that only 1000 Monte Carlo runs may not provide sufficient statistical confidence but suffice to illustrate the impact of the various system specifications here considered. For this reason, authors purposefully avoid expressing flyby accuracies through their numerical

value, and it is rather indicated whether an accuracy better than ±100 km (3σ) is possible or not. Notice, also, that simulations for asteroids with *a priori* ephemeris uncertainties >100,000 km result in flyby accuracies similar to those in Table 6, given that such large uncertainties cannot be mitigated even with larger ΔV capabilities or limiting visual magnitudes.

Table 7 can thus serve as reference to identify the system performance required to achieve accurate flybys for a particular asteroid. Results also justify the allocation of a more capable star tracker in the CubeSat design than those in off-the-shelf ADCS units (Table 2), since accurate flybys are only possible for 3 asteroids with a limiting visual magnitude of 7 (e.g., BCT's XACT unit). From these results, it is also clear that the largest improvements in flyby accuracies are obtained through larger limiting visual magnitudes. A clear example of this is that accurate flybys are feasible for up to 19 asteroids if the limiting visual magnitude is V_{lim}=15, as compared to 11 asteroids if V_{lim}=11, and 3 if V_{lim}=7.

Regarding ΔV capabilities, accurate flybys are possible for up to 15 asteroids with a larger ΔV budget of 90 m/s (i.e., >15 m/s for TCMs, affordable on 6U platforms). It is furthermore observed that no significant improvements are obtained when increasing the ΔV budget from 90 m/s to 100 m/s: accurate flybys are possible for up to 15 asteroids with both ΔV budgets, since the limiting factor eventually becomes the relative estimation error rather than the available ΔV for TCMs. Analysis therefore shows that flyby accuracies are primarily driven by the accuracy of relative navigation, whereas the available ΔV for TCMs plays a less significant role.

The same behavior is observed for more pessimistic system accuracies than those established in Table 2. As mentioned, if the requirements on thruster or ADCS performance in Table 2 cannot be fulfilled, a larger ΔV would be required for TCMs (or larger V_{lim}). For instance, if a thrust magnitude accuracy of 5% (3σ) is employed instead, a total ΔV of 110 m/s becomes necessary to achieve flyby accuracies similar to those achieved through a 1% (3σ) accuracy. And, further, if a larger ΔV is available (e.g., 120 m/s), flyby accuracies cease to improve since relative navigation accuracies become the main limiting factor. Notice also that, in principle, this ΔV may only be attained on 6U or larger CubeSats, and, conclusively, ΔV budget makes a bigger difference in terms of the total number of asteroids that can be reached from L1/L2 rather than on the flyby accuracies that can be achieved autonomously.

5.4. Effect of Minimal Ground Station Support

Relative navigation accuracies are identified in sections 5.2 and 5.3 as the main driver for autonomous CubeSat missions. However, optical observations of the target asteroids become available only a few days before the flyby. Longer asteroid visibility times could be enabled by larger exposure times or through a larger navigation camera, but challenges may still arise in terms of image processing and ADCS stability. Alternatively, minimal navigation support from ground stations could highly

increase the estimation accuracy prior to asteroid detection, and, consequently, reduce the dependence on long asteroid visibility times—although this scenario abandons the fully-autonomous mission premise.

To illustrate the effect of minimal ground-based navigation support, Monte Carlo simulations (1000 runs) are performed considering that one two-way Doppler measurement (range and range rate) is available per month (Table 8): all other system specifications are kept the same as in the baseline mission scenario (Table 2). JPL's 0.5U Iris radio [69,70] could be allocated even on 3U/6U CubeSat platforms [33], and is reported to have two-way Doppler capability of similar performance to that of traditional space missions [71]: ±1 m (1σ) and ±0.1 mm/s (1σ). Such performance is assumed in the Monte Carlo simulations, and the two-TCM guidance strategy introduced in Section 4.2.1 is employed.

It is also noted that, in this scenario, navigation accuracies prior to asteroid detection are primarily driven by the radiometric observations and not by those of the Sun and visible planets. As such, best flyby accuracies are obtained performing the first trajectory correction maneuver, TCM_1, shortly after a new radiometric observation is collected and not in between radiometric observations—given that no large improvements in navigation accuracy occur in periods when only observations of the Sun and planets are collected. Results from these Monte Carlo simulations are summarized in Table 8.

Table 8 shows that, with only minimal ground support, accurate asteroid flybys are generally possible unless *a priori* ephemeris uncertainties are large: accurate flybys are possible for all asteroids that are visible for more than 6 hours and whose *a priori* ephemeris uncertainty is below 1000 km. As such, the main limiting factor for a semi-autonomous mission becomes the *a priori* uncertainty in asteroid ephemerides rather than the limiting magnitude of the navigation camera. Accurate flybys are possible for 20 asteroids, which also represents a large improvement over the baseline mission scenario (accurate flybys were possible for 11 asteroids), and improvements are similar to those obtained through a limiting magnitude of 15 (accurate flybys were possible for 19 asteroids).

It should also be noted that, although this mission scenario is not fully autonomous, radiometric observations collected only once per month may still be able to keep ground operations costs low. In this semi-autonomous scenario, radiometric observations effectively improve the accuracy in the computation of the first trajectory correction maneuver, TCM_1, which then reduces the ΔV demand on the second correction maneuver, TCM_2. Minor limitations are still observed for cases with low ΔV available for TCMs (e.g., 2012 EY11), for long transfer times to the asteroid (e.g., 2001 FO32), and for asteroids that are visible for less than 12 hours (e.g., 2008 AG33).

Table 8
Feasibility of accurate asteroid flybys with monthly ground-based radiometric observations.

Asteroid	From	Nominal trajectory characteristics [32]		Visible days from CubeSat	Feasibility from points of minimum and maximum nominal ΔV requirement
		Time of flight (days)	ΔV range from L1/L2 (m/s)		
2005 WD	L2	141.7↔150.0	59.1↔69.2	0.8	All
2015 BK509		150.0	47.2	0.8	Large *a priori* ephemeris uncertainty
2008 TZ3		129.7↔149.9	42.5↔56.9	7.1	All
2004 UE		150.0↔137.5	39.1↔54.3	0.4	Large *a priori* ephemeris uncertainty
2017 XC62		150.0↔141.8	26.0↔60.5	2.4	All
1989 JA		142.2↔140.0	36.7↔66.3	0.4	All
1998 ST27		138.1↔109.2	23.6↔61.3	0.3	All
2008 DG5		138.0	32.8	2.6	All
1997 NC1		140.4↔81.0	15.6↔68.2	0.6	All
2012 EY11		150.0↔149.9	68.2↔73.3	12.4	Min.
2001 SQ3		140.7↔124.5	38.4↔68.3	0.6	All
2001 WN5		150.0↔115.5	44.1↔65.0	3.8	All
2011 LJ19		150.0	64.0	0.4	Large *a priori* ephemeris uncertainty
2004 OB		149.6	36.4	1.5	All
2004 MN4		140.2↔55.9	5.7↔57.6	2.5	All
2001 FO32	L1	150.0↔78.1	30.5↔62.8	2.2	Max.
2016 AJ193		138.9↔150.0	42.4↔64.7	0.3	Large *a priori* ephemeris uncertainty
2008 AG33		150.0↔150.0	16.9↔60.9	0.4	Min.
2014 HK129		150.0	47.3	18.4	All
2010 XC15		141.2	26.7	0.6	All
2018 CC14		141.6	68.5	0.6	All
2001 WN5		33.3↔149.9	4.4↔40.3	1.0	All
2011 LJ19		117.4↔95.6	15.9↔54.0	0.5	Large *a priori* ephemeris uncertainty
2009 BL71		150.0↔110.8	20.3↔50.3	0.9	All
2004 MN4		125.8↔33.3	20.9↔50.7	7.3	All

All: Accurate flyby is feasible from L1/L2 departure points with minimum and maximum nominal ΔV requirements.
Min./Max.: Accurate flyby is only feasible from L1/L2 departure point with minimum/maximum nominal ΔV requirement.

6. Conclusions

This study presents a feasibility analysis of autonomous operations on CubeSat platforms for asteroid flyby missions. The mission concept considers a CubeSat departs from a halo orbit around the Sun-Earth Lagrange points and performs autonomous navigation and guidance along the flyby trajectory. An autonomous navigation and guidance strategy is proposed, which is compatible with CubeSats' limited capabilities in terms of computational power, sensor allocation, and ΔV budget.

The navigation strategy consists of two phases: (1) observations of visible planets and of the Sun until the target asteroid becomes visible, and (2) observations of the target asteroid for relative optical navigation. The guidance strategy employs two trajectory correction maneuvers to improve flyby accuracies: one maneuver before asteroid detection, and another maneuver during the relative navigation phase. A heuristic approach to determine the time of execution of each correction maneuver is also introduced, and Monte Carlo simulations are performed to understand the flyby accuracies that can be achieved autonomously. State-of-the-art system specifications are considered as well as uncertainties in asteroid ephemerides.

Flyby accuracies well below 100 km (3σ) are found possible if the mission characteristics are suitable in terms of: (a) asteroid visibility time ($V_{lim}\geq 11$), (b) available ΔV for trajectory correction maneuvers (>15 m/s), (c) uncertainty in asteroid ephemeris prior to the mission (<1000 km), and (d) short transfer to asteroid. Results of the two-TCM guidance strategy introduced here show significant advantages over a one-TCM strategy, both in terms of flyby accuracies for a given ΔV budget, and in terms of limiting visual magnitude of the on-board navigation camera. The proposed strategy also presents advantages over more conventional approaches based on pre-scheduled maneuvers and navigation accuracy thresholds.

However, the number of asteroids for which <100-km flyby accuracies are possible is limited: 15 out of 25 analyzed asteroids (ΔV=90 m/s and $V_{lim}=11$), and improving these results would require either a larger ΔV budget to reach a larger number of asteroids, longer exposure times, a more capable navigation camera, or partial navigation support from ground stations. A high-impulse propulsion system is also seen essential provided the short-duration relative navigation phases. In support of alternative mission scenarios, the impact of different system specifications is also discussed (e.g., larger ΔV budget and various limiting visual magnitudes), as well as the impact of minimal navigation support from ground stations. The limiting magnitude of the navigation camera is shown to be the most relevant factor for a fully-autonomous mission, whereas minimal ground support (once per month) can drastically improve flyby accuracies in a semi-autonomous mission scenario: accurate flybys are possible for 20 out of 25 analyzed asteroids.

Ultimately, this study provides a detailed feasibility analysis of asteroid flyby missions using autonomous (and semi-autonomous) CubeSats. Autonomous navigation and guidance strategies are proposed and proven effective despite limited CubeSat capabilities, limitations for autonomous operations are identified, and system implications for autonomous asteroid-flyby CubeSat missions are discussed.

Acknowledgement

Funding was provided by Cranfield University's Ph.D. scholarships through their European Partnership Programme (2016–2017, United Kingdom). No official grant ID is associated to this scholarship.

References

[1] Doyle, R. J. The Emergence of Spacecraft Autonomy. 1997.

[2] Wood, L. J. The Evolution of Deep Space Navigation: 1999-2004. No. 152, 2014, pp. 827–847.

[3] Owen Jr., W. M., Duxbury, T. C., Acton Jr., C. H., Synnott, S. P., Riedel, J. E., and Bhaskaran, S. A Brief History of Optical Navigation at JPL. No. 131, 2008, pp. 329–348.

[4] Riedel, J. E., Bhaskaran, S., Desai, S., Hand, D., Kennedy, B., McElrath, T., and Ryne, M. *Deep Space 1 Technology Validation Report - Autonomous Optical Navigation (AutoNav)*. Pasadena, CA, USA, 2000.

[5] Kransner, S. M., and Bernard, D. E. Integrating Autonomy Technologies into an Embedded Spacecraft System - Flight Software System Engineering for New Millennium. No. 2, 1997, pp. 409–420 vol.2.

[6] Bhaskaran, S., Mastrodemos, N., Riedel, J. E., and Synnott, S. P. Optical Navigation for the STARDUST Wild 2 Encounter. 2004.

[7] Kubitschek, D. G., Mastrodemos, N., Werner, R. A., Kennedy, B. M., Synnott, S. P., Null, G. W., Bhaskaran, S., Riedel, J. E., and Vaughan, A. T. Deep Impact Autonomous Navigation: The Trials of Targeting the Unknown. No. 125, 2006, pp. 381–406.

[8] Kubota, T., Hashimoto, T., Kawaguchi, J., Uo, M., and Shirakawa, K. Guidance and Navigation of Hayabusa Spacecraft for Asteroid Exploration and Sample Return Mission. 2006.

[9] Tsuda, Y., Yoshikawa, M., Abe, M., Minamino, H., and Nakazawa, S. "System Design of the Hayabusa 2-Asteroid Sample Return Mission to 1999 JU3." *Acta Astronautica*, 2013. https://doi.org/10.1016/j.actaastro.2013.06.028.

[10] Polle, B., Frapard, B., Gil-Fernández, J., Milic, E., Graziano, M., Rebordão, J., and Motrena, P. Autonomous Navigation for Interplanetary Missions Performance Achievements Based on Real and Flight Images. 2006.

[11] Christian, J. A. "Optical Navigation Using Planet's Centroid and Apparent Diameter in Image." *Journal of Guidance, Control, and Dynamics*, Vol. 38, No. 2, 2014, pp. 192–204. https://doi.org/10.2514/1.G000872.

[12] Raymond Karimi, R., and Mortari, D. "Interplanetary Autonomous Navigation Using Visible Planets." *Journal of Guidance, Control, and Dynamics*, Vol. 38, No. 6, 2015, pp. 1151–1156. https://doi.org/10.2514/1.G000575.

[13] Du, S., Wang, M., Chen, X., Fang, S., and Su, H. "A High-Accuracy Extraction Algorithm of Planet Centroid Image in Deep-Space Autonomous Optical Navigation." *Journal of Navigation*, Vol. 69, No. 4, 2016, pp. 828–844. https://doi.org/10.1017/S0373463315000910.

[14] Ning, X., Gui, M., Zhang, J., Fang, J., and Liu, G. "Solar Oscillation Time Delay Measurement Assisted Celestial Navigation Method." *Acta Astronautica*, Vol. 134, 2017, pp. 152–158. https://doi.org/10.1016/j.actaastro.2017.01.039.

[15] Dahir, A., Kubitschek, D., and Palo, S. Recovering Time and State for Autonomous Navigation Systems in Deep Space. No. 164, 2018, pp. 433–442.

[16] Christian, J. A. "StarNAV: Autonomous Optical Navigation of a Spacecraft by the Relativistic Perturbation of Starlight." *Sensors*, Vol. 19, No. 19, 2019, p. 4064. https://doi.org/10.3390/s19194064.

[17] Chen, X., Sun, Z., Zhang, W., and Xu, J. "A Novel Autonomous Celestial Integrated Navigation for Deep Space Exploration Based on Angle and Stellar Spectra Shift Velocity Measurement." *Sensors (Basel, Switzerland)*, Vol. 19, No. 11, 2019, p. 2555. https://doi.org/10.3390/s19112555.

[18] Ray, P. S., Sheikh, S. I., Graven, P. H., Wolff, M. T., Wood, K. S., and Gendreau, K. C. Deep Space Navigation Using

Celestial X-Ray Sources. No. 1, 2008, pp. 101–109.

[19] Wang, Y., Zheng, W., and Sun, S. "X-Ray Pulsar-Based Navigation System/Sun Measurement Integrated Navigation Method for Deep Space Explorer." *Proceedings of the Institution of Mechanical Engineers, Part G: Journal of Aerospace Engineering*, Vol. 229, No. 10, 2014, pp. 1843–1852. https://doi.org/10.1177/0954410014561705.

[20] Shemar, S., Fraser, G., Heil, L., Hindley, D., Martindale, A., Molyneux, P., Pye, J., Warwick, R., and Lamb, A. "Towards Practical Autonomous Deep-Space Navigation Using X-Ray Pulsar Timing." *Experimental Astronomy*, Vol. 42, No. 2, 2016, pp. 101–138. https://doi.org/10.1007/s10686-016-9496-z.

[21] Rowell, N., Parkes, S., and Dunstan, M. "Image Processing for Near Earth Object Optical Guidance Systems." *IEEE Transactions on Aerospace and Electronic Systems*, Vol. 49, No. 2, 2013, pp. 1057–1072. https://doi.org/10.1109/TAES.2013.6494399.

[22] Pellacani, A., Kicman, P., Suatoni, M., Casasco, M., Gil, J., and Carnelli, I. "Design and Validation of a GNC System for Missions to Asteroids: The AIM Scenario." *CEAS Space Journal*, Vol. 10, No. 4, 2018, pp. 555–566. https://doi.org/10.1007/s12567-017-0189-x.

[23] Baldini, F., Harvard, A., Chung, S.-J., Nesnas, I., and Bhaskaran, S. Autonomous Small Body Mapping and Spacecraft Navigation. No. 2018-Octob, 2018.

[24] Pesce, V., Agha-Mohammadi, A.-A., and Lavagna, M. Autonomous Navigation & Mapping of Small Bodies. No. 2018-March, 2018, pp. 1–10.

[25] Chan, D. M., and Agha-Mohammadi, A.-A. Autonomous Imaging and Mapping of Small Bodies Using Deep Reinforcement Learning. No. 2019-March, 2019.

[26] Mody, A. A., Barad, K., and Loganathan, M. Autonomous Navigation: Optical State Acquisition Systems for Lunar and Interplanetary Small Satellites. 2016.

[27] Sharma, T., Barad, K. R., Mody, A. A., and Shanmukh, R. S. G. Autonomous Navigation: Accommodating Pulsar Based Navigation System in Small-Micro Class Satellites. 2017.

[28] Segret, B., Hestroffer, D., Quinsac, G., Agnan, M., Vannitsen, J., and Mosser, B. In-Flight Orbit Determination for a Deep Space CubeSat. 2018.

[29] Modenini, D., Zannoni, M., Manghi, R. L., and Tortora, P. "An Analytical Approach to Autonomous Optical Navigation for a CubeSat Mission to a Binary Asteroid System." *Advances in the Astronautical Sciences*, Vol. 163, No. October, 2018, pp. 139–149.

[30] Schwartz, S., Nallapu, R. T., Gankidi, P., Dektor, G., and Thangavelautham, J. Navigating to Small-Bodies Using Small Satellites. 2018.

[31] Franzese, V., Di Lizia, P., and Topputo, F. "Autonomous Optical Navigation for the Lunar Meteoroid Impacts Observer." *Journal of Guidance, Control, and Dynamics*, 2019, pp. 1–8. https://doi.org/10.2514/1.g003999.

[32] Machuca, P., Sánchez, J. P., Masdemont, J. J., and Gómez, G. "High-Fidelity Trajectory Design to Flyby Near-Earth Asteroids Using CubeSats." *Acta Astronautica*, Vol. 167, 2020, pp. 146–163. https://doi.org/10.1016/j.actaastro.2019.09.041.

[33] Machuca, P., Sánchez, J. P., and Greenland, S. "Asteroid Flyby Opportunities Using Semi-Autonomous CubeSats: Mission Design and Science Opportunities." *Planetary and Space Science*, Vol. 165, 2019, pp. 179–193. https://doi.org/10.1016/j.pss.2018.11.002.

[34] Palo, S., Stafford, G., and Hoskins, A. An Agile Multi-Use Nano Star Camera for Constellation Applications. 2013.

[35] Jørgensen, J. L., Denver, T., Betto, M., Jørgensen, P. S., Kurnaz, S., Ince, F., and Onbassioglu, S. The Bering Autonomous Target Detection. 2003.

[36] Pezent, J. B., Sood, R., and Heaton, A. Near Earth Asteroid (NEA) Scout Solar Sail Contingency Trajectory Design and Analysis. 2018.

[37] Strange, N., Asphaug, E., Grogan, K., Landau, D., and Reh, K. *Planetary Science Decadal Survey - Near Earth Asteroid Trajectory Opportunities in 2020-2024*. Pasadena, CA, USA, 2010.

[38] Campagnola, S., Ozaki, N., Sugimoto, Y., Tam, C. H., Chen, H., Kawabata, Y., Ogura, S., Sarli, B., Kawakatsu, Y., Funase, R., and Nakasuka, S. Low-Thrust Trajectory Design and Operations of PROCYON, the First Deep-Space Micro-Spacecraft. 2015.

[39] Greco, C., Di Carlo, M., Walker, L., and Vasile, M. Analysis of NEOs Reachability with Nano-Satellites and Low-Thrust Propulsion. 2018.

[40] Domingo, V., Fleck, B., and Poland, A. I. "The SOHO Mission: An Overview." *Solar Physics*, 1995. https://doi.org/10.1007/BF00733425.

[41] McNamara, P., and Racca, G. *Introduction To LISA Pathfinder*. 2009.

[42] Pilbratt, G. L. *The Herschel Mission, Scientific Objectives, and This Meeting*. 2001.

[43] Tauber, J. A. "The Planck Mission." *Advances in Space Research*, 2004. https://doi.org/10.1016/j.asr.2003.05.025.

[44] Prusti, T., de Bruijne, J. H. J., Brown, A. G. A., and Vallenari, A. "The Gaia Mission." *Astronomy and Astrophysics*, 2016. https://doi.org/10.1051/0004-6361/201629272.

[45] ESA. *ARIEL - Assessment Study Report*. 2017.

[46] ESA. *PLATO - Definition Study Report*. 2017.

[47] NASA. *Wide-Field InfrarRed Survey Telescope-Astrophysics Focused Telescope Assets WFIRST-AFTA 2015 Report*.

2015.

[48] Space Telescope Science Institute. *James Webb Space Telescope Project*. Greenbelt, MD, USA, 2004.

[49] Sergeyevsky, A., Snyder, G., and Cunniff, R. *Interplanetary Mission Design Handbook, Volume I, Part 2. Earth to Mars Ballistic Mission Opportunities, 1990-2005*. Pasadena, CA, USA, 1983.

[50] Mason, J. P., Baumgart, M., Rogler, B., Downs, C., Williams, M., Woods, T. N., Palo, S., Chamberlin, P. C., Solomon, S., Jones, A., Li, X., Kohnert, R., and Caspi, A. "MinXSS-1 CubeSat On-Orbit Pointing and Power Performance: The First Flight of the Blue Canyon Technologies XACT 3-Axis Attitude Determination and Control System." *Journal of Small Satellites*, 2017.

[51] Jørgensen, J. L., Liebe, C. C., Eisenmann, A., and Jensen, G. B. "The Advanced Stellar Compass Onboard the Oersted Satellite." *Spacecraft Guidance, Navigation and Control Systems*, Vol. 381, 1997, p. 303.

[52] Riis, T., and Jørgensen, J. L. Tracking Non-Stellar Objects on Ground and in Space. 1999.

[53] Hyperion Technologies B.V. *Hyperion Technologies SS200 Sun Sensor*. Delft, Netherlands, 2017.

[54] Armano, M., Audleyb, H., Augerc, G., Bairdn, J., Binetruyc, P., Bornb, M., and Bortoluzzid, D. "A Strategy to Characterize the LISA-Pathfinder Cold Gas Thruster System." *Journal of Physics*, Vol. Conference, No. 610, 2015. https://doi.org/10.1088/1742-6596/610/1/012026.

[55] Tapley, B., and Ingram, D. "Orbit Determination in the Presence of Unmodeled Accelerations." *IEEE Transactions on Automatic Control*, Vol. 18, No. 4, 1973, pp. 369–373. https://doi.org/10.1109/TAC.1973.1100331.

[56] Franzese, V., Di Lizia, P., and Topputo, F. "Autonomous Optical Navigation for LUMIO Mission." *2018 Space Flight Mechanics Meeting*, No. January, 2018. https://doi.org/10.2514/6.2018-1977.

[57] Gupta, A. K., and Song, D. "Lp-Norm Spherical Distribution." *Journal of Statistical Planning and Inference*, Vol. 60, No. 2, 1997, pp. 241–260. https://doi.org/https://doi.org/10.1016/S0378-3758(96)00129-2.

[58] Gates, C. R. *A Simplified Model of Midcourse Maneuver Execution Errors.* Jet Propulsion Laboratory, Pasadena, Calif., 1963.

[59] Ku, H. H. "Notes on the Use of Propagation of Error Formulas." *Journal of Research of the National Bureau of Standards*, Vol. 70C, No. 4, 1966, pp. 263–273.

[60] NASA. JPL HORIZONS. http://ssd.jpl.nasa.gov/?horizons. Accessed Jan. 1, 2018.

[61] European Space Agency. NEODyS-2. https://newton.spacedys.com/neodys/. Accessed Jan. 15, 2019.

[62] Lagerkvist, C.-I., and Magnusson, P. "Analysis of Asteroid Lightcurves. II. Phase Curves in a Generalized HG-System." *Astronomy and Astrophysics Supplement Series*, Vol. 86, No. 2, 1990, pp. 119–165.

[63] Bowell, E., Hapke, B., Lumme, K., Harris, A. W., Domingue, D., and Peltoniemi, J. "Application of Photometric

Models to Asteroids." *Asteroids II*, No. June, 1988, pp. 524–556.

[64] Boattini, A., D'Abramo, G., Scholl, H., Hainaut, O. R., Boehnhardt, H., West, R., Carpino, M., Hahn, G., Michelsen, R., Forti, G., Pravec, P., Valsecchi, G. B., and Asher, D. J. "Near Earth Asteroid Search and Follow-up beyond 22nd Magnitude: A Pilot Program with ESO Telescopes." *Astronomy and Astrophysics*, Vol. 418, No. 2, 2004, pp. 743–750. https://doi.org/10.1051/0004-6361:20034428.

[65] European Southern Observatory. Observing with ESO Telescopes. https://www.eso.org/sci/observing.html. Accessed Oct. 15, 2019.

[66] Desmars, J., Bancelin, D., Hestroffer, D., Thuillot, W., Desmars, J., Bancelin, D., Hestroffer, D., Statistical, W. T., Desmars, J., Bancelin, D., Hestro, D., and Thuillot, W. "Statistical and Numerical Study of Asteroid Orbital Uncertainty." *Astronomy and Astrophysics*, Vol. A32, No. 554, 2013.

[67] Wiesel, W. E. *Modern Orbit Determination*. Aphelion Press, Beavercreek, OH, USA, 2003.

[68] Taylor, J. The Deep Space Network: A Functional Description. In *Deep Space Communications*, Jet Propulsion Laboratory, NASA, Pasadena, CA, USA, 2014, pp. 15–36.

[69] Duncan, C. B., Smith, A. E., and Aguirre, F. H. Iris Transponder – Communications and Navigation for Deep Space. 2014.

[70] NASA. *Iris V2 CubeSat Deep Space Transponder*. Pasadena, CA, USA, 2015.

[71] Angkasa, K. S., Border, J. S., Duncan, C. B., Kobayashi, M., Towfic, Z. J., and Voss, T. J. "Regenerative Ranging for JPL Software-Defined Radios." *IEEE Aerospace and Electronic Systems Magazine*, Vol. 34, No. 10, 2019, pp. 46–55. https://doi.org/10.1109/MAES.2019.2911002.

[72] Thornton, C. L., and Border, J. S. *Radiometric Tracking Techniques for Deep-Space Navigation*. Pasadena, CA, USA, 2000.

[73] Morley, T., and Budnik, F. Rosetta Navigation for the Fly-by of Asteroid 2867 Šteins. 2009.

[74] Gelb, A., Kasper, J. F., Nash, R. A., Price, C. F., and Sutherland, A. A. *Applied Optimal Estimation*. The M.I.T. Press, 1974.

[75] Schiff, C. Adapting Covariance Propagation to Account for the Presence of Modeled and Unmodeled Maneuvers. In *AIAA/AAS Astrodynamics Specialist Conference and Exhibit*, American Institute of Aeronautics and Astronautics, 2006.

[76] Kawabata, B. Y., and Kawakatsu, Y. "On-Board Orbit Determination Using Sun Sensor and Optical Navigation Camera for Deep-Space Missions." Vol. 15, 2017, pp. 13–19.

[77] VACCO Industries. *VACCO Green Propulsion System*. South El Monte, CA, USA, 2019.

2021-08-18

CubeSat autonomous navigation and guidance for low-cost asteroid flyby missions

Machuca, Pablo

American Institute of Aeronautics and Astronautics

Machuca P, Sánchez J-P. (2021) CubeSat autonomous navigation and guidance for low-cost asteroid flyby missions. Journal of Spacecraft and Rockets, Available online 18 August 2021 https://doi.org/10.2514/1.A34986